COMPUTATIONALLY EFFICIENT AND ROBUST NON-LINEAR 3D CYCLIC MODELING OF RC STRUCTURES THROUGH A HYBRID FINITE ELEMENT MODEL (HYMOD)

George Markou[1*], Christos Mourlas[2] and Manolis Papadrakakis[3]

[1*]Department of Civil Engineering, Universidad Católica de la Santísima Concepción, Alonso de Ribera 2850, Concepción, Chile

e-mail: markou@ucsc.cl

[2,3]Department of Civil Engineering, National Technical University of Athens, GR-54124, Greece

e-mail: mourlasch@central.ntual.gr[2], mpapadra@central.ntua.gr[3]

Keywords: Hybrid Finite Elements, Cyclic Loading, Reinforced Concrete, Smeared Crack Approach, Embedded Rebars.

Abstract

A computationally efficient and robust simulation method is presented in this work, for the cyclic modeling of reinforced concrete (RC) structures. The proposed hybrid modeling (HYMOD) approach alleviates numerical limitations regarding the excessive computational cost during the cyclic analysis and provides a tool for the detailed simulation of the 3D cyclic nonlinear behavior of full-scale RC structures. The simplified HYMOD approach is integrated in this work with a computationally efficient cyclic concrete material model so as to investigate its numerical performance under extreme cyclic loading conditions. The proposed approach adopts a hybrid modeling concept that combines hexahedral and beam-column finite elements, where the coupling between them is achieved through the implementation of kinematic constraints. A parametric investigation is performed through the use of the Del Toro Rivera frame joint and two RC frames with a shear wall. The proposed modeling method managed to decrease the computational cost in all numerical tests performed in this work, while it induced additional numerical stability during the cyclic analysis, where the required number of internal iterations per displacement increment was found to be always smaller compared to the unreduced (hexahedral) model. The HYMOD provides for the first time with the required 3D detailed finite element solution tools in order to simulate the nonlinear cyclic response of full-scale RC structures without hindering the numerical accuracy of the derived model nor the need of developing computationally expensive models that practically cannot be solved through the use of standard computer systems.

1. Introduction

The cyclic loading simulation of different structural components of reinforced concrete (RC) buildings such as beams, columns, monolithic connections, shear walls, slabs and foundation footings, has two main challenges; numerical accuracy and computational efficiency. Many simplified models have been developed for the simulation of RC structural members under ultimate limit state and cyclic loading conditions with moderate success. The accuracy limitations of these numerical models is well documented thus researchers turned towards more detailed 3D approaches (Kotsovos and Pavlovic, 1995; Hartl, 2002; Lykidis and Spiliopoulos, 2008; Červenka and Papanikolaou, 2008; Papanikolaou and Kappos, 2009; Markou and Papadrakakis, 2013; Ali et al., 2016, Mourlas et al., 2017) in an attempt to develop accurate and robust modeling methods that will be able to predict the mechanical response of any RC structural member or structure. These research studies adopt the use of hexahedral elements that treat cracks through the use of the smeared crack approach and model rebars as embedded rod or beam finite elements.

As it was concluded by Markou and Papadrakakis (2015), the computational complexity of such

detailed models makes their use impractical for simulation of real-scale RC structures. Additionally, the use of numerically unstable material models, such as the smeared crack approach in concrete (Markou and Papadrakakis, 2013), increases the numerical sensitivity to various user-defined parameters. Therefore, there is a need of developing a more robust and numerically efficient finite element modeling approach that will alleviate the abovementioned numerical limitations for simulating full-scale RC structures under ultimate limit state monotonic and cyclic conditions, without loses in-terms of accuracy and at the same time achieving computational efficiency.

A mixed element formulation was reported in Formaggia et al. (2001), Urquiza et al. (2006) and Blanco et al. (2007), in an attempt to deal with the connection of plates and 3D solid elements, which was extended to the connection of shells and solid elements by Huang (2004). Nazarov (1996, 1999) and Kozlov and Maz'ya (2001) presented an asymptotic analysis for the coupling between a 3D elastic body and a dimensionally reduced structure. The coupling of models of different dimensionality, from a purely kinematical point of view, were explored in Formaggia et al. (2001), Urquiza et al. (2006) and Blanco et al. (2007). Blanco et al. (2008) presented a generalized approach on the kinematic coupling of incompatible elements. Mata et al. (2008) used two different FE models (3D solid and 1D beam elements), where the structure was initially discretized with beam elements and when predefined regions entered the nonlinear state, they were assumed prismatic and were discretized with 3D solid elements. Bournival et al. (2010a, 2010b) used mixed-dimensional FEA models for the simulation of steel structures, combining beam, shell and 3D solid finite elements. According to their research work, it was reported that they managed to reduce the computational effort at the expense of losing the accuracy across the interface of the incompatible finite elements.

When dealing with the cyclic loading of RC structural members, the computational demand increases significantly, while there were no research publications in the international literature that attempt to implement any type of hybrid model for the prediction of the cyclic response of RC structures.

The proposed HYMOD approach for modeling RC structures under ultimate limit cyclic loading requires minimal transformations for the coupling demands of line and 3D elements, maximizes the computational efficiency during the analysis, while maintaining an adequate accuracy in calculating the internal forces at the critical regions of the structure. In addition to that, the adopted concrete material model (Mourlas et al. 2017) requires the definition of a minimum number of material parameters so as to describe and simulate the nonlinear mechanical behavior of concrete under cyclic loading conditions, which significantly simplifies the procedure of material model definition.

2. Concrete Material Modeling

Given that the HYMOD approach (Markou and Papadrakakis, 2015) considers two different types of FE simulations that their formulation is based on one- and three-dimensional models, two different material models are adopted herein. For the case of the 1D natural beam column flexibility-based (NBCFB) fiber element, the model foresees the discretization of each beam-column section through the use of fibers that have the ability to account for nonlinearities through the use of the bilinear model (see Fig. 1), while for all analyses performed in this research work the hardening modulus was set to zero.

For the 3D simulation, the Kotsovos and Pavlovic (1995) material model is incorporated into the 8-noded hexahedral elements for the nonlinear cyclic analysis of concrete structures (Mourlas et al. 2017). Furthermore, a flexible crack closure criterion was integrated that induces numerical stability during the analysis. According to the cyclic concrete material model presented in (Mourlas et al. 2017), the smeared crack approach described in (Markou and Papadrakakis, 2013) is used to simulate the crack openings in the case of the 3D detailed model. This approach was first presented by Rashid (1968) and then implemented by Gonzalez-Vidosa et al. (1991). Smeared crack models take into consideration crack openings by modifying the stiffness matrices and stresses at the corresponding integration points (Fig. 2). This approach proceeds with the simulation of individual cracks without the need for remeshing, as it is required for the case of the discrete-crack approach, where a physical

gap is introduced in the FE mesh at the location of the crack.

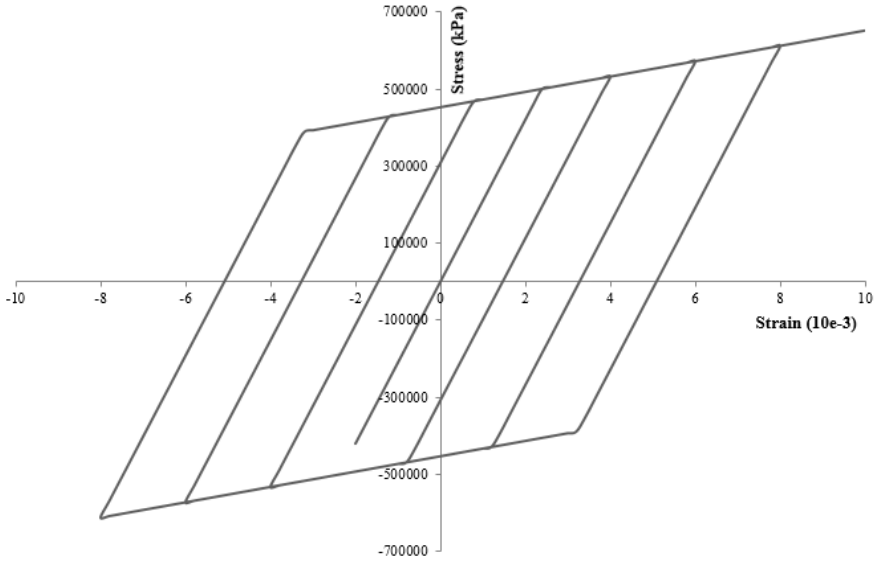

Figure 1. Bilinear model for cyclic analysis.

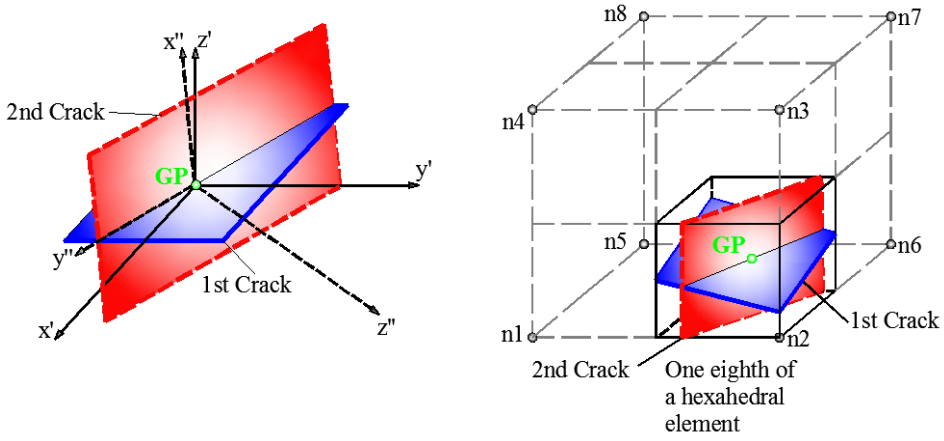

Figure 2. Local axes for the case of two cracks at a specific Gauss point. (Markou and Papadrakakis, 2013)

The Kotsovos and Pavlovic (1995) material model is described by the use of the bulk modulus, the shear modulus and an equivalent external stress σ_{id}. The bulk and the shear modulus describe the volume and the distortional changes in the material, while the stress σ_{id} takes into account the coupling effect between deviatoric stress and volumetric variation. For the mathematical description of the constitutive model, each state of stress and strain is decomposed into hydrostatic and deviatoric components. The hydrostatic and deviatoric octahedral expressions of stresses (σ_0, τ_0) and strains ($\varepsilon_{0(h)}$, $\varepsilon_{0(d)}$, γ_0) are used in the constitutive relations (h and d stand for hydrostatic and deviatoric components, respectively). According to the above, the σ_{id} describes the coupling effect of τ_0-$\varepsilon_{0(d)}$. The constitutive relations are presented below:

$$\varepsilon_0 = \varepsilon_{0(h)} + \varepsilon_{0(d)} = (\sigma_0 + \sigma_{id}) / (3K_s) \quad (1)$$

$$\gamma_0 = \gamma_{0(d)} = \tau_0 / (2G_s) \quad (2)$$

where, K_s and G_s are the secant forms of bulk and shear moduli, respectively. Analytical expressions of the secant modulus, shear modulus and σ_{id} are derived by regression analysis of the experimental data in Kotsovos and Pavlovic (1995). These material properties are expressed as functions of current state of stress (σ_0, τ_0, f_c).

By using the generalized form of Hooke's law in the expression (Markou and Papadrakakis, 2015), the following formula derives (in order to define the strains in global coordinate directions):

$$\varepsilon_{ij} = (\sigma_{ij} + \sigma_{id}\delta_{ij}) / (2G_s) - (3v_s / E_s)(\sigma_0 + \sigma_{id})\delta_{ij} \quad (3)$$

where, E_s (σ_o, τ_o, f_c) and ν_s (σ_o, τ_o, f_c) are the secant Young's modulus and Poisson's ratio, respectively, derived from *Ks* and *Gs* by the following standard formulae of linear elasticity:

$$E_s = (9K_sG_s)/(3K_s+G_s)\ ,\ \nu_s = (3K_s-2G_s)/(6K_s+2G_s) \tag{4}$$

The stress and strain increments are determined by using the tangent expressions of modulus K_t, G_t, E_t, ν_t during the nonlinear iterative procedure and the hydrostatic correction σ_{id}.

In the present work the unified total crack approach (UTCA) proposed by Lykidis and Spiliopoulos (2008) is adopted. The UTCA approach that was also implemented in Markou and Papadrakakis (2013, 2015), foresees that the state of crack formation or closure is treated in a unified way within every Newton-Raphson internal iteration.

The numerical procedure is based on the brittle nature of concrete. Therefore, when the criterion of failure is satisfied, there is an abrupt loss of strength capacity of the concrete material point. The strength envelope of concrete is expressed by the value of the ultimate deviatoric stress by using the expressions of Willam and Warkne (1974):

$$\tau_{0u} = \frac{2\tau_{0c}(\tau_{0c}^2-\tau_{0e}^2)\cos\theta + \tau_{0c}(2\tau_{0e}-\tau_{0c})\sqrt{4(\tau_{0c}^2-\tau_{0e}^2)\cos^2\theta + 5\tau_{0e}^2 - 4\tau_{0c}^2\tau_{0e}^2}}{4(\tau_{0c}^2-\tau_{0e}^2)\cos^2\theta + (2\tau_{0e}-\tau_{0c})^2} \tag{5}$$

where, the rotational variable θ defines the deviatoric stress orientation on the octahedral plane. The τ_{0e} *(θ=0°)* and τ_{0c} *(θ=60°)* correspond to the state of $\sigma_1=\sigma_2>\sigma_3$ (triaxial extension) and $\sigma_1>\sigma_2=\sigma_3$ (triaxial compression), respectively. The analytical expressions of τ_{0e} and τ_{0c} are derived from experimental data. It must be noted at this stage that, the tensile strength and the shear retention factor are variables of the material model that can be directly defined within the model, as described in Mourlas et al. (2017).

The smeared crack approach treats cracking by redistributing the cracked stresses to the uncracked areas. Therefore, the model prevents the eccentric concentration of stress in the cracked areas, which may lead to numerical instabilities. Thus, when a crack is formed, the stresses are calculated through the following expression:

$$\boldsymbol{\sigma}_{Cr} = \boldsymbol{T}^{-1}\begin{bmatrix} \boldsymbol{\sigma}_1 = 0 \\ \boldsymbol{\sigma}_2 \\ \boldsymbol{\sigma}_3 \\ 0 \\ 0 \\ 0 \end{bmatrix} \tag{6}$$

where, $\boldsymbol{T}^{-1}$ is the inverse transformation matrix that is used to transform the principal stress axes to the initial x, y and z axes.

Additionally, the proposed procedure uses a flexible crack closing criterion introduced in Mourlas et al. (2017), which is crucial in cyclic loading conditions. A numerical investigation presented in Mourlas et al. (2017), shows that during unloading conditions the strains, which are directed orthogonal to the crack plane, are getting much smaller than the value of strains that cause the crack formation. From a numerical point of view, this phenomenon is explained by the values of strains normal to the crack that are getting much lower than the values of strains causing the formation of cracking. Therefore, the proposed criterion for the closure of cracks (Mourlas et al. 2017) is expressed as follows:

$$\varepsilon_i \le \left(b - \frac{n_{cr}-1}{n_{tot}}\right)\varepsilon_{cr} \tag{7}$$

where, ε_i is the current strain in the i-direction, which is normal to the crack plane and ε_{cr} is the strain

that caused the crack formation. Parameter *b* is the number of the imposed displacement branch of the load history (i.e. Fig. 3 shows 2 imposed displacement branches; equal to a half loading cycle), n_{cr} and n_{tot} are the numbers of increment that the crack is formed and the total number of increments that an imposed displacement branch is divided into, respectively. A schematic representation of the variables that are shown in Eq. 7, is illustrated through Fig. 3, which is an example of a half loading cycle. Each branch is divided into 40 displacement increments. The y-axis consists of the number of increments (where the $d^{ext.}$ is the total external imposed displacement and the Δd^{incr} is the imposed displacement of each incremental iteration), while the x-axis represents the number of loading cycles.

Hence, when a crack is closed at the i-Newton-Raphson iteration, the elastic constitutive matrix D_{el} is used to calculate the stresses of the previously cracked Gauss point by using the following expression:

$$\boldsymbol{\sigma}^{i} = \boldsymbol{\sigma}^{i-1} + \boldsymbol{D}_{el}\boldsymbol{\Delta\varepsilon}^{i} \tag{8}$$

The adopted constitutive behavior of the concrete material at a Gauss point for both cracked and uncracked states are described in the Mourlas et al. (2017).

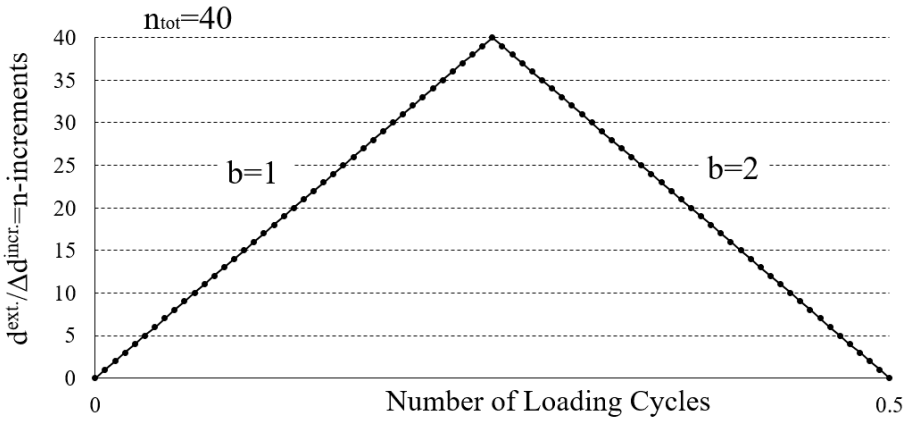

Figure 3. Schematic representation of b and n_{tot} variables of Eq. 7, for a half loading cycle.

3. Modeling of Rebar Elements

Reinforcement steel bars are modeled as embedded rod or beam elements within the 8-noded isoparametric hexahedral elements, as implemented by Markou and Papadrakakis (2015). The material of steel-reinforcement is modeled through the use of the Menegotto-Pinto (1973) model that takes into account the Bauschinger effect. The stress-strain relation takes the form:

$$\sigma^{*} = b\varepsilon^{*} + \frac{(1-b)\varepsilon^{*}}{(1+\varepsilon^{*R})^{1/R}} \tag{9}$$

where, $\varepsilon^{*} = (\varepsilon - \varepsilon_r)/(\varepsilon_0 - \varepsilon_r)$, $\sigma^{*} = (\sigma - \sigma_r)/(\sigma_0 - \sigma_r)$ and $R = R_0 - a_1\xi/(\alpha_2 + \xi)$.

The parameter b is the strain hardening ratio between E_0 and E_t, while ε_0 and σ_0 are the coordinates of the point where the asymptotes of the branch intersect and (ε_r, σ_r) are the coordinates of the point, where the last strain reversal with stress increment of equal sign takes place. The parameter R is a decreasing function of ξ, which is the strain difference between the current asymptote intersection point and the previous load reversal point with maximum or minimum strain, depending on whether the corresponding steel stress at reversal is positive or negative. Parameters R_0, a_1 and a_2 are experimentally determined and assumed in this study to be 20, 18.5 and 0.15, respectively.

4. Hybrid Modeling Formulation - Kinematical Coupling of 1D and 3D Finite Elements

According to the proposed HYMOD approach that was presented in Markou and Papadrakakis (2015), the method combines hexahedral and beam-column finite elements, where the coupling between them is achieved through kinematic constraints. The coupling between the two types of

elements (natural beam-column flexibility-based "NBCFB" and hexahedral "HEXA" finite elements) is performed with kinematic constraints, which are enforced at each hexahedral node, located at the interface between the beam and the solid elements, as follows:

$$\underset{(3x1)}{\boldsymbol{u}_i^{HEXA}} = \underset{(3x6)}{\boldsymbol{T}_{im}} \cdot \underset{(6x1)}{\boldsymbol{u}_m^{NBCFB}}, \tag{10}$$

with

$$\underset{(3x6)}{\boldsymbol{T}_{im}} = \begin{bmatrix} 1 & 0 & 0 & 0 & z_i - z_m & y_m - y_i \\ 0 & 1 & 0 & z_m - z_i & 0 & x_i - x_m \\ 0 & 0 & 1 & y_i - y_m & x_m - x_i & 0 \end{bmatrix} \tag{11}$$

Therefore, Eq. 10 takes the following form;

$$\begin{bmatrix} u_i \\ v_i \\ w_i \end{bmatrix} = \begin{bmatrix} 1 & 0 & 0 & 0 & z_i - z_m & y_m - y_i \\ 0 & 1 & 0 & z_m - z_i & 0 & x_i - x_m \\ 0 & 0 & 1 & y_i - y_m & x_m - x_i & 0 \end{bmatrix} \begin{bmatrix} u_1^{NBCFB} \\ v_1^{NBCFB} \\ w_1^{NBCFB} \\ \theta_1^{NBCFB} \\ \varphi_1^{NBCFB} \\ \psi_1^{NBCFB} \end{bmatrix} \tag{12}$$

where $\boldsymbol{u}_m^{NBCFB}$ and $\boldsymbol{u}_i^{HEXA}$ are the displacement vectors of the NBCFB node corresponding to 6 dof and the hexahedral nodes (3 dof per node) at the interface, respectively. The subscript *i* of the global coordinates (x, y, z), refers to the hexahedral node ID located at the interface section $\boldsymbol{\Omega}_i^1$, while subscript *m* refers to the NBCFB elemental node ID that controls the displacements (master node) of the interface section $\boldsymbol{\Omega}_i^1$ (see Fig. 4). The connection matrix $\boldsymbol{T}_{im}$ is computed from the compatibility conditions of NBCFB and hexahedral nodal coordinates.

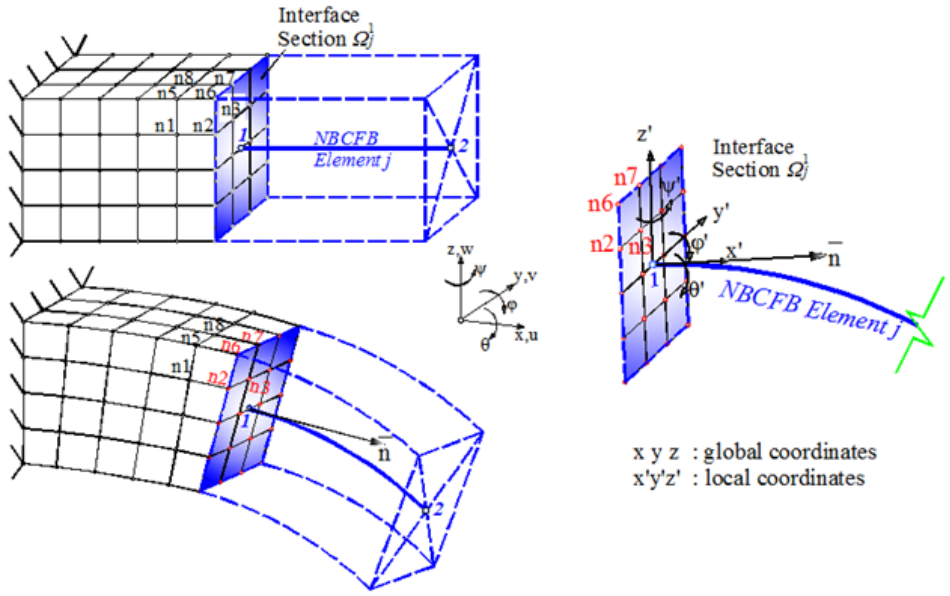

Figure 4. Kinematic constraints imposed by the 1D structural member on the interface section $\boldsymbol{\Omega}_i^1$. (Markou and Papadrakakis, 2015)

If we assume that a hexahedral node is located at the interface of a NBCFB and hexahedral elements, it should follow the body movements of section $\boldsymbol{\Omega}_i^1$, which are enforced by the NBCFB element nodal translational and rotational displacements (as shown in Fig. 4). Therefore, the computation of the new position for any point on the interface section $\boldsymbol{\Omega}_i^1$ is obtained through a linear

transformation as follows:

$$\underset{(24x1)}{\boldsymbol{U}^{\text{HEXA}}} = \underset{(24x18)}{\boldsymbol{T}_H} \cdot \underset{(18x1)}{\boldsymbol{U}^{hybrid}} \tag{13}$$

For computing the transformation matrix $\boldsymbol{T}_H$, the coordinates of the slave nodes that are controlled by the kinematic constraints and the x_m, y_m, z_m coordinates of the corresponding master node are required. The transformation matrix $\boldsymbol{T}_H$ is used for the purpose of obtaining the 18x18 transformed stiffness matrix of any hybrid hexahedron, according to Eq. 14, while the nodal displacements of the slave nodes are computed according to Eq. 13.

$$\underset{(18x18)}{\boldsymbol{K}_H^{\text{HEXA}}} = \underset{(18x24)}{\boldsymbol{T}_H^T} \cdot \underset{(24x24)}{\boldsymbol{K}^{\text{HEXA}}} \underset{(24x18)}{\boldsymbol{T}_H} \tag{14}$$

The calculation of the internal forces of the transformed hexahedral elements is performed as follows:

$$\underset{(18x1)}{\boldsymbol{F}_H} = \underset{(18x24)}{\boldsymbol{T}_H^T} \cdot \underset{(24x1)}{\boldsymbol{F}^{\text{HEXA}}} \tag{15}$$

where $\boldsymbol{F}_H$ is the internal force vector of the transformed hexahedral element. More details on the kinematic constraints can be found in Markou and Papadrakakis (2015).

5 Numerical Investigation and Discussion

The numerical analysis results will be presented in this section for the case of three models that were selected for the purpose of this research work. The first is the Del Toro Rivera (1988) frame joint that is used herein to demonstrate the ability of the proposed HYMOD algorithm to capture accurately experimental results and how its accuracy is being affected when different HYMOD reduction levels are used. The other two models (1- and 2-storey RC frames) are used to demonstrate the computational efficiency of the proposed modeling approach in solving numerically demanding problems with significant shear nonlinearities and excessive cracking. It must be noted at this point that the nonlinear solution strategy used to perform the analyses discussed in this section, was the Newton-Raphson displacement control algorithm in connection to a work-based convergence criterion (Eq. 16). The general convergence tolerance that was used for all the numerical nonlinear analyses (where it is not stated) was 10^{-4} in order to achieve a high accuracy and induce additional stability during the cyclic nonlinear analysis. The CPU used to perform all the analyses presented in this work had a 3.7 GHz computing power.

$$\boldsymbol{e}_{err} = \frac{\boldsymbol{\Delta u}_s^j \left\| \boldsymbol{F}_s^{t+\Delta t} - \boldsymbol{R}_s^{t+\Delta t} \right\|}{\boldsymbol{\Delta u}_s^1 \left\| \boldsymbol{F}_s^{t+\Delta t} - \boldsymbol{R}_s^{t} \right\|} \leq 10^{-4} \tag{16}$$

5.1 Del Toro Rivera RC Frame Joint

Fig. 5 illustrates the schematic representation of the under study RC frame joint that was tested by Del Toro Rivera (1988). According to the experiment's design, the uniaxial compressive concrete strength of the joint was f_c = 40 MPa and the corresponding yielding stresses of the steel reinforcement were 570, 490, 440 and 554 MPa for the 10, 12, 14 and 20 mm diameter bars, respectively. The Young modulus of elasticity of the reinforcement steel was E_S = 200 GPa, which was also the material parameter used in this numerical investigation. The strength under tension was set to 5% of the uniaxial compressive strength, while the shear retaining factor β was set equal to 0.05 in all numerical models.

The under study interior frame joint was subjected to different cyclic loading conditions according to the experimental setup (Del Toro Rivera, 1988). The loading history is presented in the form of imposed displacements in Fig. 6. It is important to note here that the joint was also loaded with a

vertical load of 200 kN at the point of the applied displacement (see Fig. 5) so as to simulate the effect of the superstructure's loads. Therefore, the stress state conditions that were developed within the joint region were highly complex given that a combination of normal and extreme shear strains were developed during the experimental test. This is also one of the main reasons why this experimental setup was selected in order to demonstrate the numerical and computational capabilities of the proposed algorithm in capturing experimental results under extreme cyclic loading conditions.

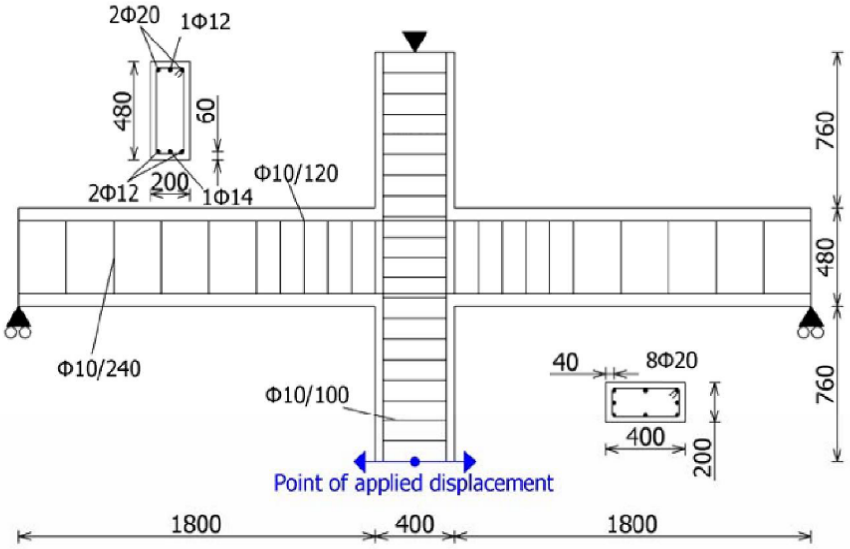

Figure 5. Geometry and reinforcement details of the Del Toro Rivera (1988) beam column joint. All dimensions are in mm.

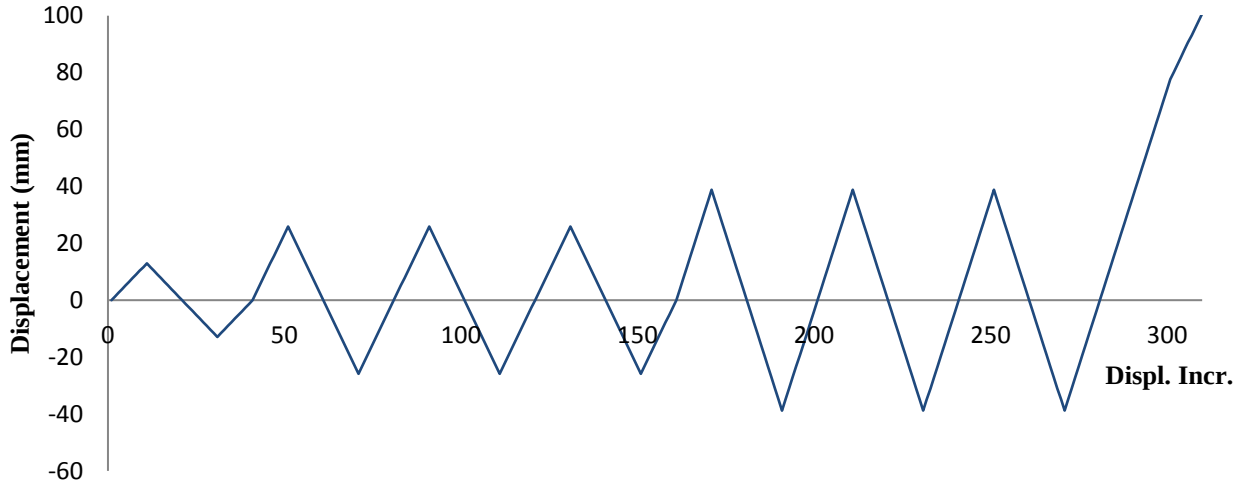

Figure 6. Load history presented in the form of imposed displacements for Del Toro Rivera beam column joint.

For the development of the numerical model, the concrete domain was discretized with 8-noded hexahedral finite elements and the steel reinforcement was discretized with the NBCFB and rod finite elements. The steel bars that had 12, 14 and 20 mm diameter were modeled through the use of beam elements and the steel bars that had 10 mm diameter were modeled through the use of rod finite elements. The frame joint was initially discretized with a total number of 76 concrete hexahedral finite elements (20cm x 20cm x 16cm) and 446 embedded steel elements were used so as to discretize the steel reinforcement, as shown in Fig. 7. After the development of the initial model that consisted of only hexahedral elements, the three HYMOD meshes were constructed accordingly (see Fig. 8).

As it can be seen in Fig. 8, the HYMOD 1 mesh corresponds to the modeling of two thirds of the horizontal beams of the joint with the NBCFB element and the remaining joint is discretized with

HEXA elements (one NBCFB element was used for each structural beam member). The model was additionally reduced in HYMOD 2 so as to further study the performance and numerical stability of the proposed algorithm, in which half of the upper column is modeled by hexahedral elements and the other half by one NBCFB element. In the last mesh (model HYMOD 3), the same discretization concept that was implemented in HYMOD 2 was considered, where both vertical structural members of the specimen were reduced thus one NBCFB element was used to model the half of each column (upper and lower). Table 1 shows the FE mesh details as they resulted from the reduction of the initial hexahedral model.

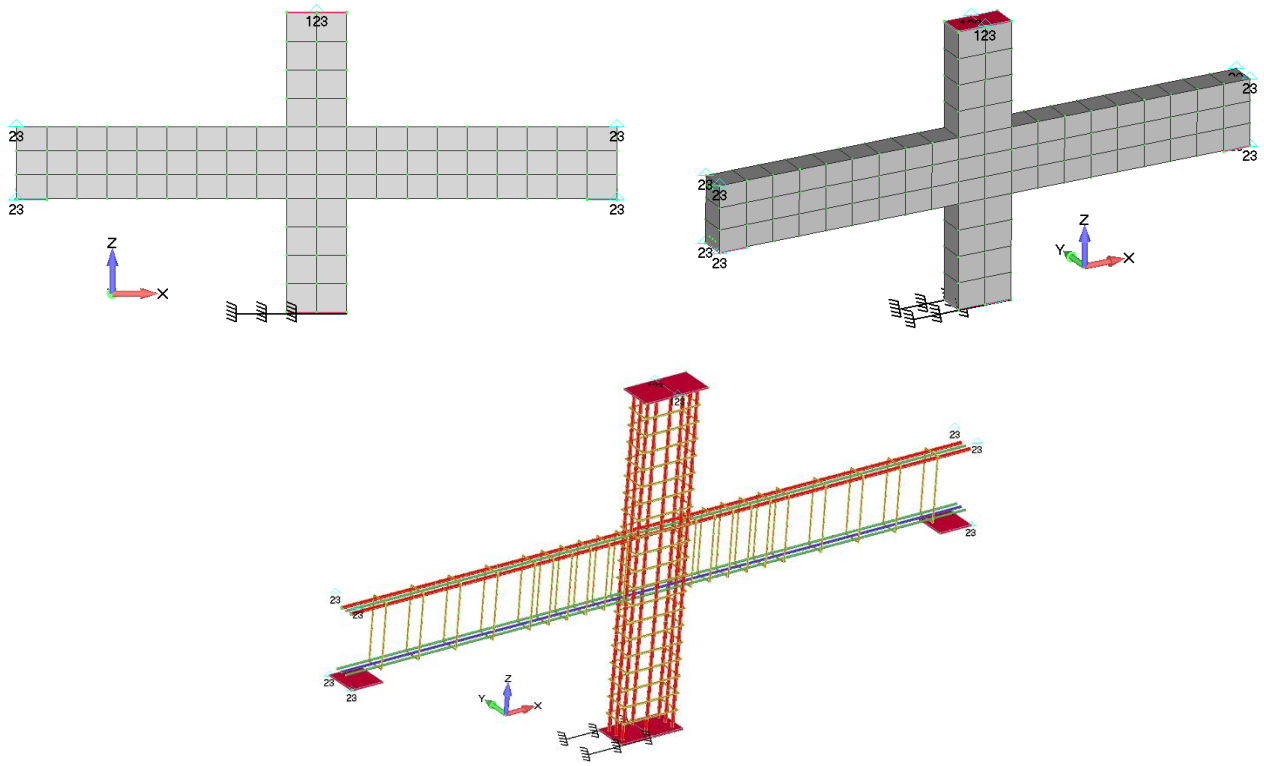

Figure 7. 2D and 3D views of the FE mesh of concrete elements and steel reinforcement embedded rebars.

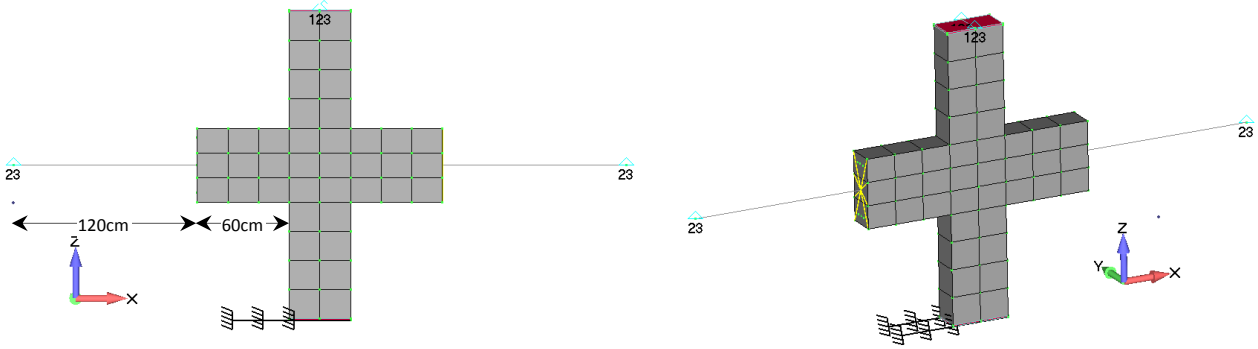

HYMOD 1.

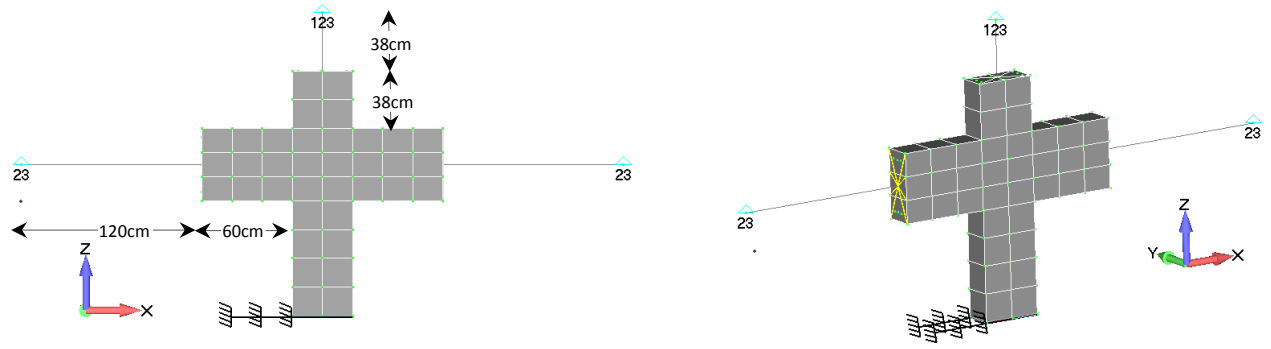

HYMOD 2.

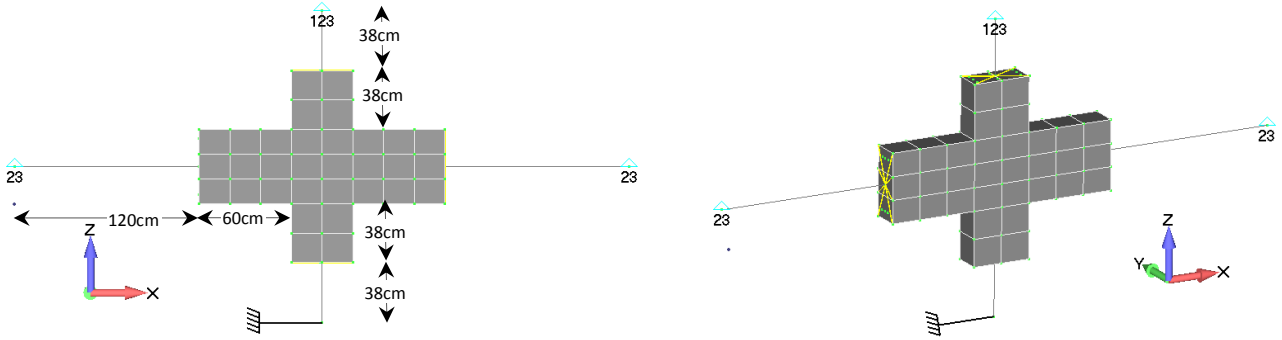

HYMOD 3.

Figure 8. 2D and 3D views of the FE meshes of the three HYMOD models.

According to the parametric investigation performed in Markou and Papadrakakis (2015), a length between h-2h, where h refers to the height of the section, was found to be adequate in order to determine the optimum plastic hinge length that has to be modeled with the hexahedral finite element. This rule was also applied herein for the case of the mesh of HYMOD 1, while for the other two meshes this rule is not valid, given that the two vertical structural elements foresee a plastic hinge length of 38 cm, which is equal to a 0.95h. Even though the minimum hinge length is not satisfied, the models were not modified in an attempt to further test the computational robustness and the numerical accuracy of the proposed algorithm.

Table 1 FE mesh details of the frame joint model.

a/a	Model	Hexahedral Elements	Embedded Rebar Elements	RC NBCFB Elements	Total Number of Dof	Dof Reduction (%)
1	Full Hexa	76	446	-	686	-
2	HYMOD 1	40	330	2	362	47
3	HYMOD 2	36	296	3	305	56
4	HYMOD 3	32	262	4	245	64

Fig. 9 illustrates the comparison between the experimental and numerical results for the case of the Full Hexa model. The diagram shows the complete force-displacement history as it was computed from the nonlinear solution of 310 displacement increments. As it can be seen in Fig. 9 and Table 2, the numerical results match very well with the experimental ones, while the average magnitude of the difference between the numerical and experimental load data per cycle was found to be equal to 11%, for both negative and positive maximum displacements. Given that the derived curves are rather complicated and difficult to graphically compare, the numerically predicted curve (Full Hexa) will be used herein as the base of comparison with the corresponding HYMOD numerical results in order to graphically present the numerical performance of the proposed algorithm.

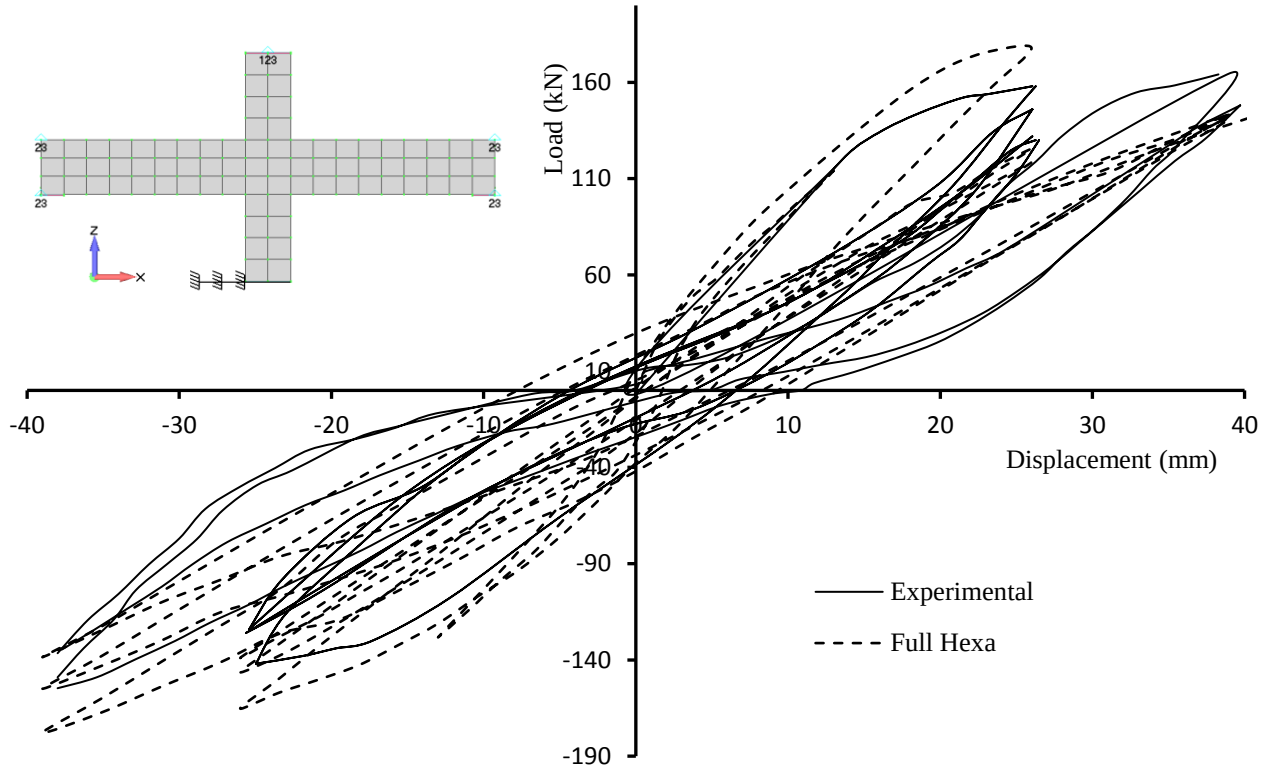

Figure 9. Frame Joint. Comparison between numerical and experimental results. Complete force-displacement history.

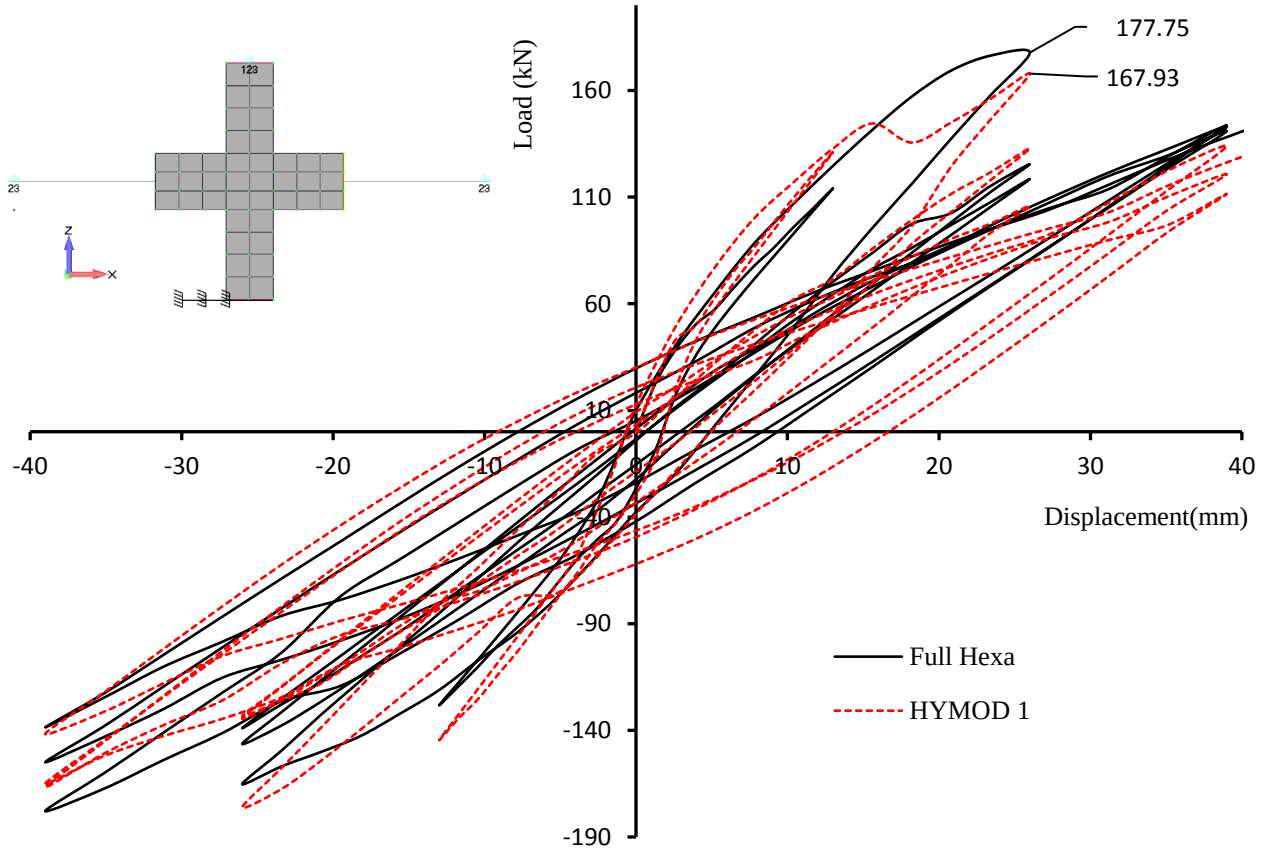

Figure 4. Frame Joint. Comparison between Full Hexa and HYMOD 1 numerical results. Complete force-displacement history.

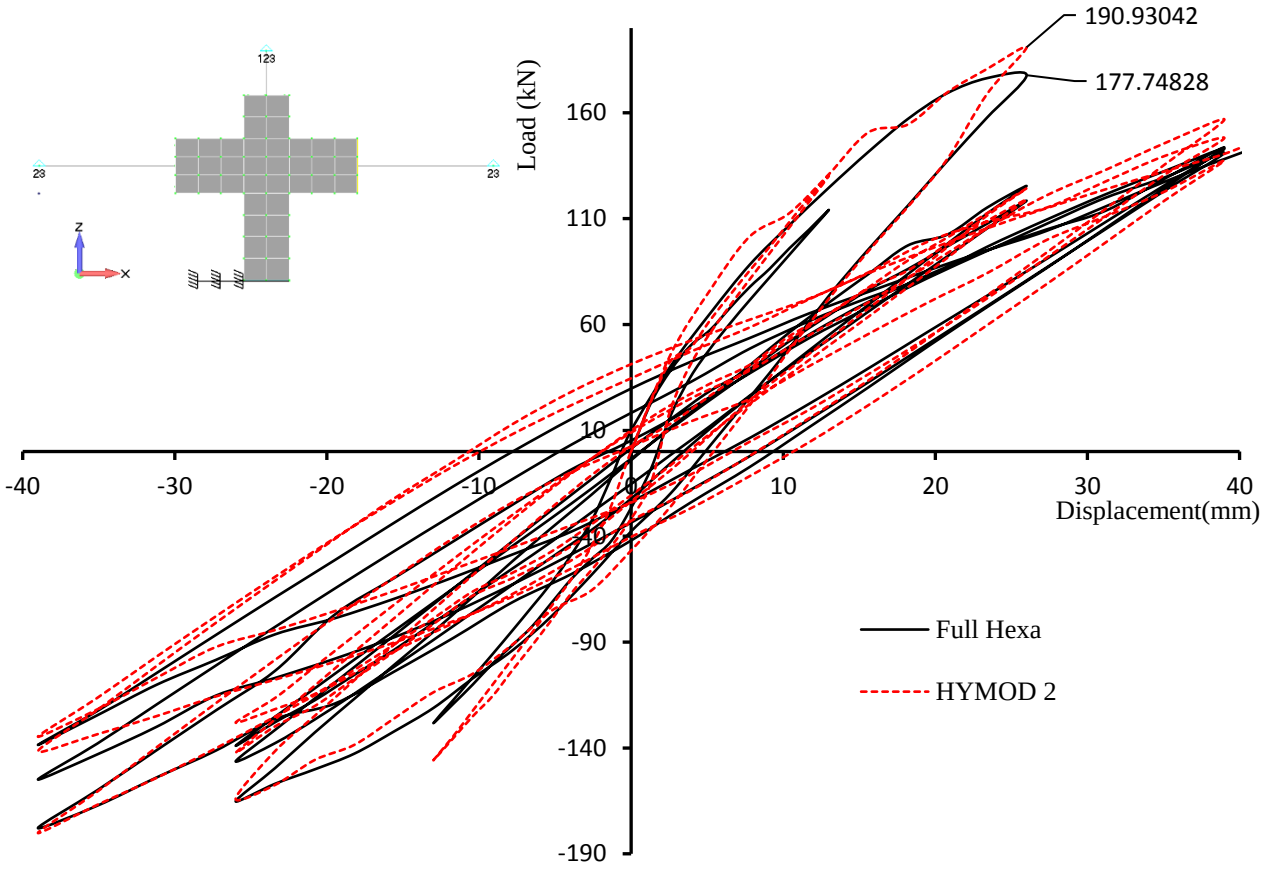

Figure 5. Frame Joint. Comparison between Full Hexa and HYMOD 2 numerical results. Complete force-displacement history.

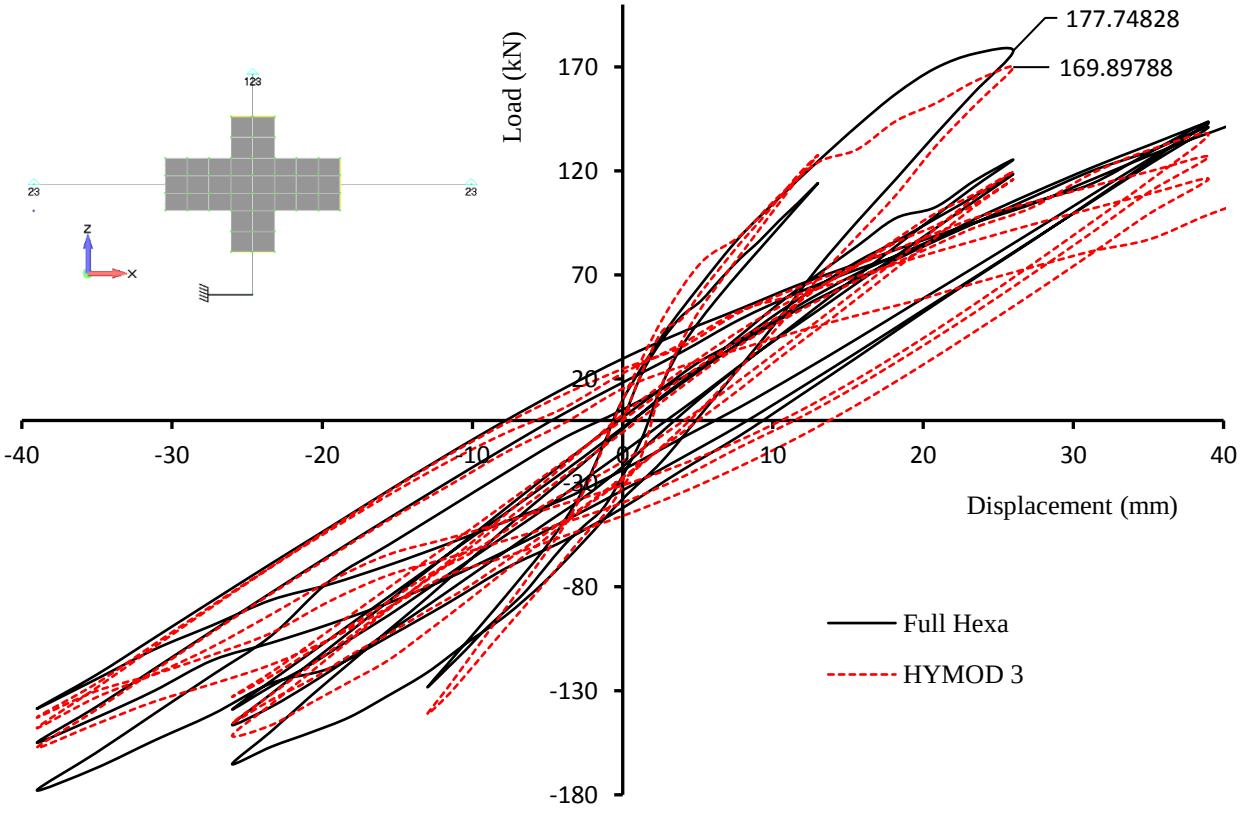

Figure 6. Frame Joint. Comparison between Full Hexa and HYMOD 3 numerical results. Complete force-displacement history.

Figs. 10-12, depict the complete force-displacement history of the three hybrid models, where the numerical results are compared with the response predicted by the Full Hexa model. As it can be seen from the three diagrams, the HYMOD models manage to capture the cyclic response with an adequate accuracy with regards to the full model. HYMOD 2 was found to be the model that had the closest numerical response with almost similar hysteretic loops with the ones obtained from the full model (see Fig. 11), while the HYMOD 3 managed to attain the closest maximum load (169.9 kN) to the one obtained from the Full Hexa model (177.75 kN). According to Tables 3 and 4, the horizontal load of each cycle of the numerical model HYMOD 2 was found to derive almost identical response with the one that was obtained from the Full Hexa model (Table 2).

Table 2 Full Hexa numerical results. Comparison of the horizontal load for each cycle.

Loading Cycle	Horizontal Load Experimental (kN)		Horizontal Load Predicted Full Hexa (kN)		Difference from experimental Full Hexa	
	Positive	Negative	Positive	Negative	Positive (%)	Negative (%)
1st	158	-142	177	-165	12.03	16.20
2nd	146	-126	125	-146	14.38	15.87
3rd	130	-124	118	-139	9.23	12.10
4th	164	-154	144	-178	12.20	15.58
5th	164	-154	141	-155	14.02	0.65
6th	149	-137	143	-139	4.03	1.46
				Average	10.98	10.31

Table 3 HYMOD 1 and 2 numerical results. Comparison of the horizontal load for each cycle.

Loading Cycle	Horizontal Load HYMOD 1 (kN)		Horizontal Load HYMOD 2 (kN)		Difference from Full Hexa-HYMOD 1		Difference from Full Hexa-HYMOD 2	
	Positive	Negative	Positive	Negative	Positive (%)	Negative (%)	Positive (%)	Negative (%)
1st	167.93	-171.22	190.93	-164.09	5.12	3.77	7.87	0.55
2nd	132.85	-134.55	124.30	-142.39	6.28	7.84	0.56	2.47
3rd	105.82	-133.46	119.00	-128.00	10.32	3.98	0.85	7.91
4th	134.00	-166.69	156.82	-180.18	6.94	6.36	8.90	1.23
5th	111.50	-165.08	137.46	-141.65	20.92	6.51	2.51	8.61
6th	120.73	-141.71	148.11	-134.69	15.58	1.95	3.57	3.10
				Average	10.86	5.07	4.05	3.98

Table 4 HYMOD 3 numerical results. Comparison of the horizontal load for each cycle.

Loading Cycle	Horizontal Load Predicted HYMOD 3 (kN)		Difference from Full Hexa-HYMOD 3	
	Positive	Negative	Positive (%)	Negative (%)
1st	169.90	-152.62	4.01	7.50
2nd	119.71	-132.87	4.23	9.00
3rd	115.94	-145.57	1.75	4.72
4th	137.63	-147.94	4.42	16.89
5th	126.84	-142.82	10.04	7.86
6th	116.15	-157.40	18.78	13.24
		Average	7.21	9.87

In order to further compare the numerically obtained results, Figs. 13 and 14 are shown herein, where the von Mises strain contours for the displacement increment in the first and sixth loading cycles can be depicted, respectively. Fig. 13 illustrates the von Mises strain contours for the case of load increments 10 and 30. It must be stated here that, each displacement cycle was divided into 10

displacement increments, therefore, for each imposed loading cycle the algorithm had to solve 40 displacement increments. The imposed maximum displacements at the tip of the column for the 1st cycle were +13 mm and -13 mm, respectively, along the x-axis. The von Mises contours illustrate the ability of the three HYMODs to capture the strain state within the solid joint without any numerical problems. It is also notable that the HYMODs developed a higher strain concentration within the hexahedral domain when compared to the contour obtained from the full Hexa model. As explained by Markou and Papadrakakis (2015), this numerical phenomenon is attributed to the stiffness difference between the NBCFB and hexahedral elements, where the beam FE is stiffer in this case forcing the more flexible domain that is discretized with hexahedrons, to develop higher strains. Nevertheless, the proposed algorithm manages to capture the overall behavior in a robust and accurate manner. In addition to that, the three HYMODs gave an almost identical von Mises strain contours.

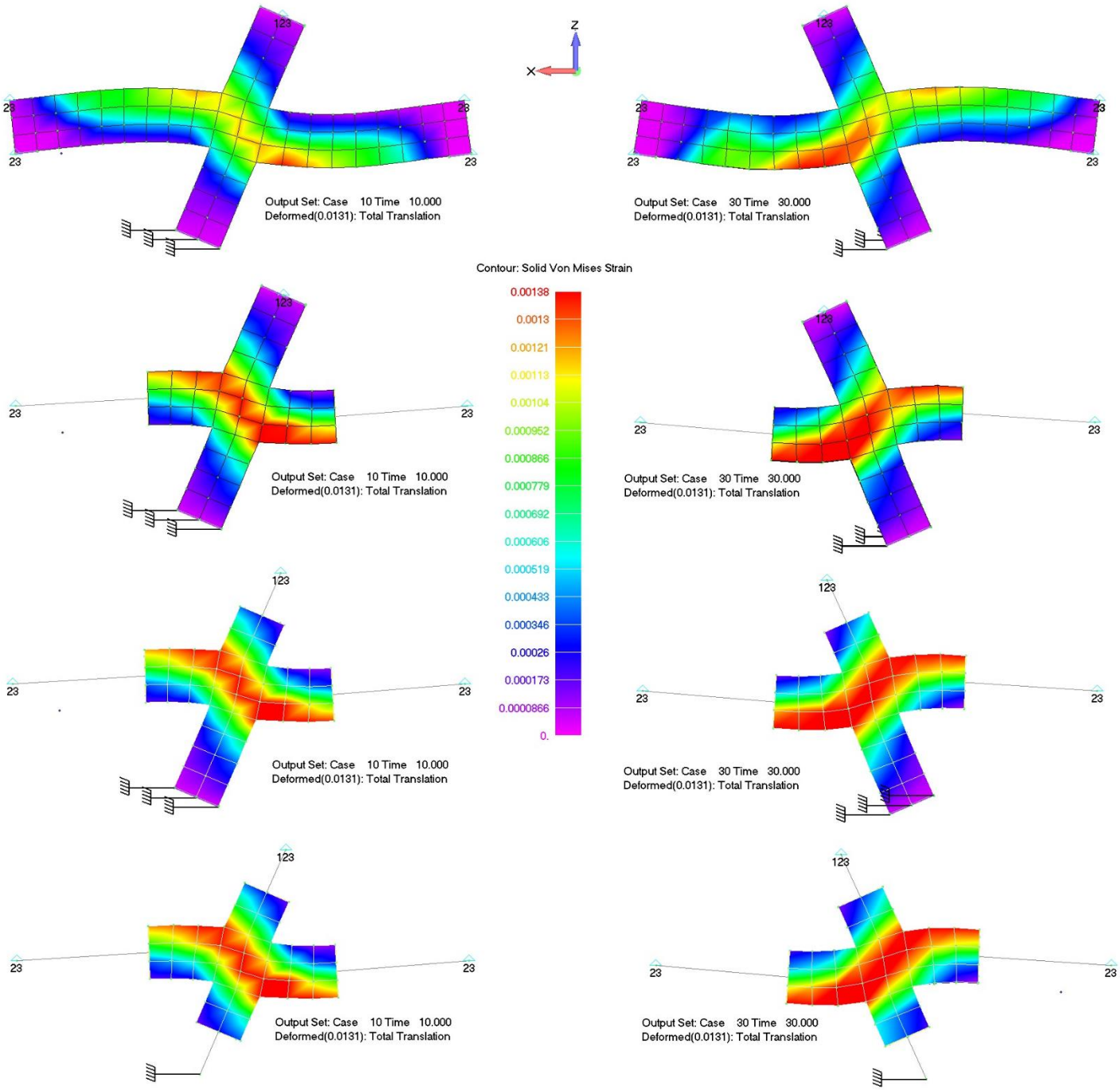

Figure 7. Frame Joint. von Mises strain contour at displacement increment 10 and 30 (1st cycle of loading). Maximum x-axis displacement: ±13 mm.

.

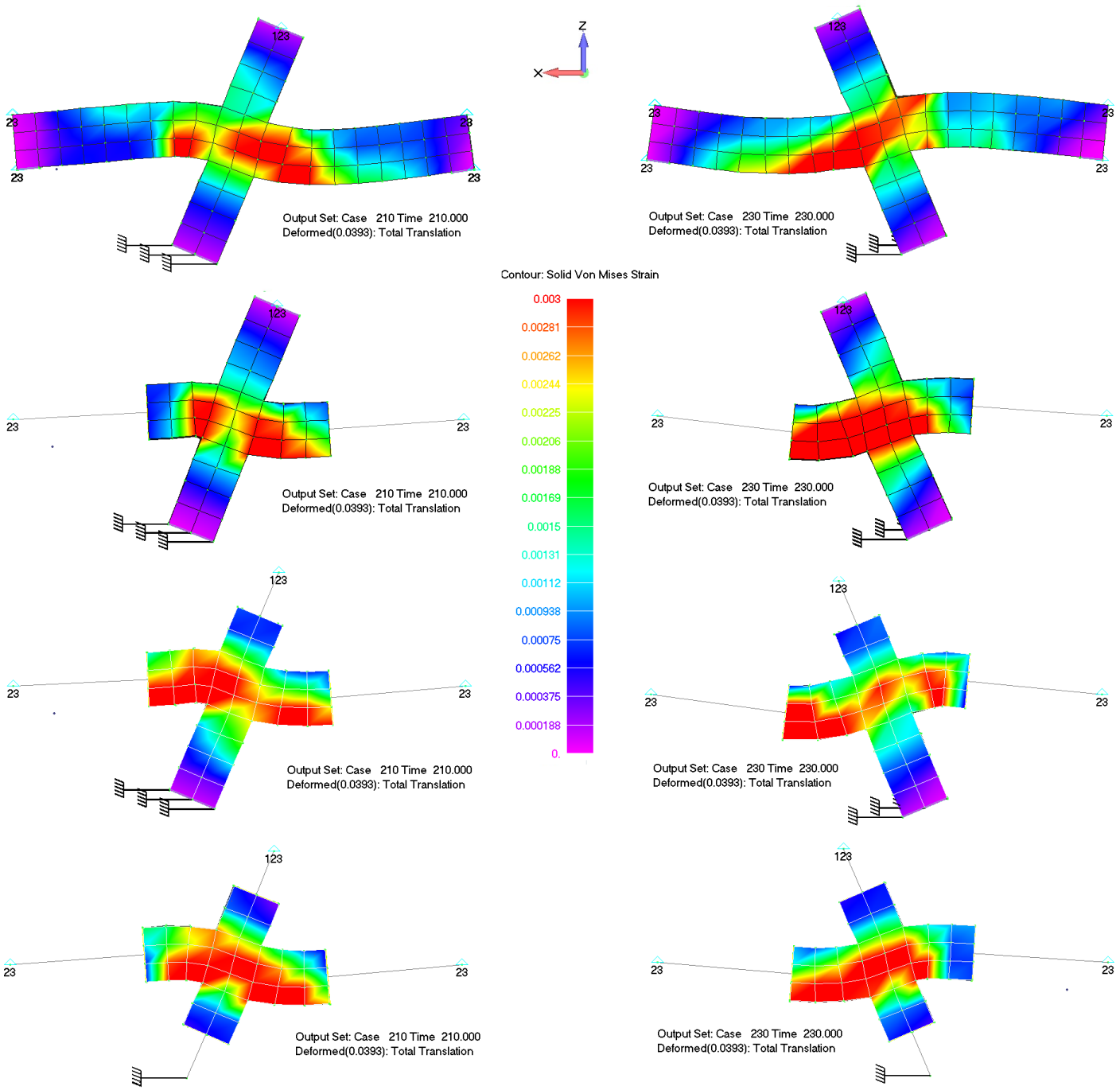

Figure 8. Frame Joint. Von Mises strain contour at displacement increments 210 and 230 (6^{th} cycle of loading). Maximum x-axis displacement: ±39 mm.

Fig. 14 illustrates the von Mises strain contours that were obtained from the four models, for the displacement increments 210 and 230. In this case, it is easy to observe that the deformation shape of the four models is the same, while the von Mises strain contours are more disturbed when it comes to this extreme deformation stage. At this point, the specimen has undergone 6 complete cycles, where it has already developed significant cracking. Therefore, the nonlinear analysis algorithm has updated the stiffness matrix several times at this stage, while the crack opening and closing was performed hundreds of times within the joint area at the Gauss points located within this domain. The numerical differences that were observed in the obtained results that derived from the HYMOD meshes are mainly attributed to the use of the NBCFB element within the HYMOD mesh that induces additional stiffness in the numerical models that force the domains that are discretized with hexahedral FEs to

develop larger deformations. Nevertheless, this numerical phenomenon does not affect significantly the overall accuracy of the under study modeling method.

Table 5 Computational performance of the four frame joint models.

a/a	Model	Num. of Displ. Incr.	Total Internal Iter.	Average Numerical Error	CPU Time Nonlinear Solution (sec)	Reduction in CPU Nonlinear Solution (%)	Reduction of Overall CPU Time (%)
1	Full Hexa	310	1052	1.94×10^{-5}	11.5	-	-
2	HYMOD 1	310	856	6.77×10^{-6}	5.9	48.7	35.22
3	HYMOD 2	310	827	8.00×10^{-6}	5.3	53.91	41.09
4	HYMOD 3	310	787	7.51×10^{-6}	5.2	54.78	48.67

Table 5 shows the CPU times required to solve the nonlinear numerical problems of the four numerical models. It is evident that the HYMODs exhibit a numerical stability that decreases the required internal iterations per displacement increment. HYMOD 3 required a total of 787 internal iterations to achieve convergence during the 310 displacement increments, while the Full Hexa model required 1,052 internal iterations. The HYMODs 1 and 2 required 856 and 827 internal iterations, respectively. The reduction regarding the CPU time required to solve the nonlinear problem, was found to be proportional to the reduction of the dofs in each model. This underlines the numerical advantage in terms of computational stability, when the HYMOD is deployed, even in the case of extreme cyclic loading conditions where the stress-strain fields are highly complex thus derive increased numerical stability demands.

In order to investigate the mesh sensitivity of the proposed algorithm, two denser meshes were used for the discretization of the frame joint. Fig. 15 shows the meshes that were constructed and their corresponding HYMODs that were used so as to study the numerical response in terms of mesh sensitivity of the HYMOD algorithm. As it can be seen in this figure, only the first level (Markou and Papadrakakis, 2015) of reduction (HYMOD 1) was performed in order to reduce the required number of analyses that will be presented herein without losing the objectivity of the performed parametric investigation. Table 6 shows the FE mesh details of the four refined models that were constructed for the mesh sensitivity analysis. As it can be seen, the overall dof reduction that derived, after the level 1 reduction scheme implementation, was approximately 48% in both refined models.

Table 6 FE mesh details of the frame joint model used for the mesh sensitivity analysis.

a/a	Model	Hexahedral Elements	Embedded Rebar Elements	RC NBCFB Elements	Total Number of Dof	Dof Reduction (%)
1	Full Hexa 1	152	710	-	1,298	-
2	HYMOD 1.1	80	454	2	674	48.07
3	Full Hexa 2	304	910	-	1,955	-
4	HYMOD 2.1	160	598	2	1,001	48.80

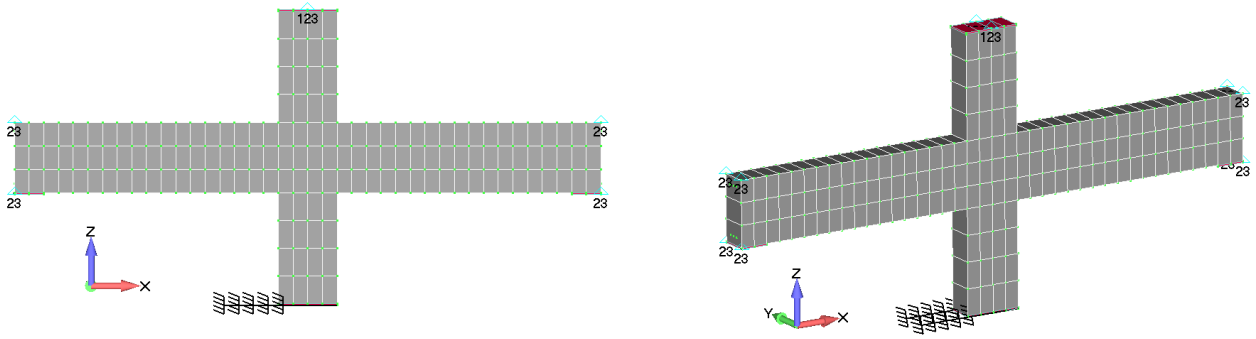

Full Hexa 1.

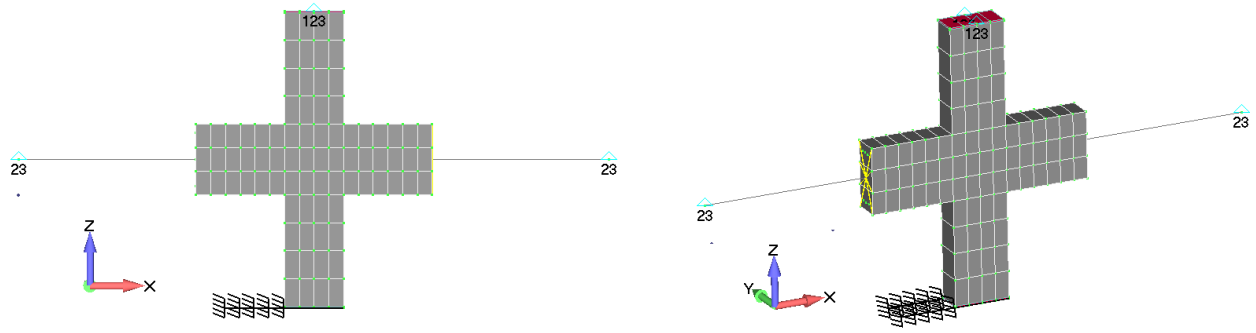

HYMOD 1.1.

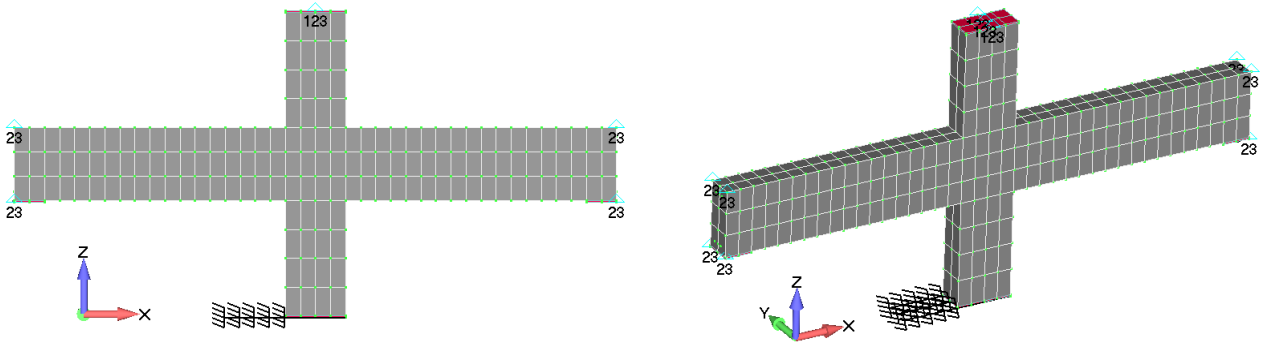

Full Hexa 2.

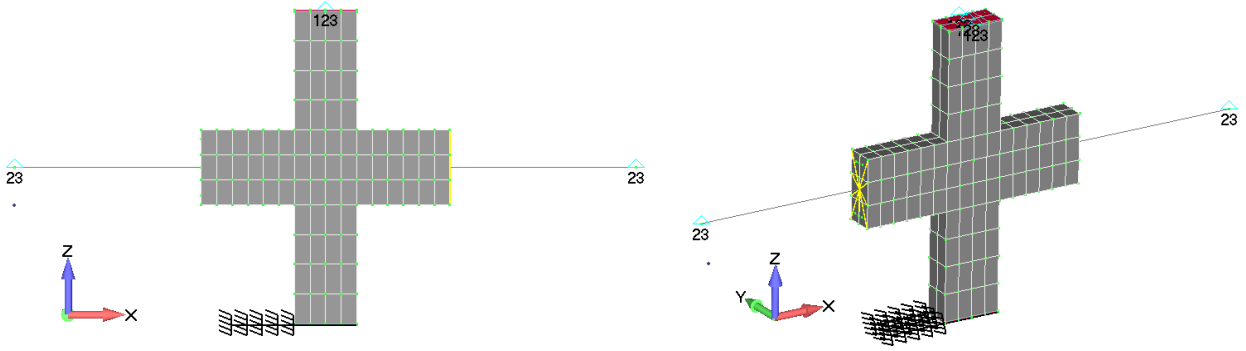

HYMOD 1.2.

Figure 9. 2D and 3D views of the FE mesh of the concrete elements used during the mesh sensitivity analysis.

Figs. 16-19 show the comparison between the experimental results and the four refined models presented in Fig. 15 and Table 6. It can be seen that all models managed to capture the experimental results thus the accuracy of the proposed algorithm is not affected by the mesh refinement in this case. Tables 7 and 8 show that the Full Hexa1, Full Hexa2 and HYMOD 1.2 managed to obtain almost similar response in terms of the horizontal load with very good agreement with the experimental ones (<10% deviation from the experimental values). The horizontal loads derived from HYMOD 1.1 present the biggest discrepancy of all the models (20%) compared to the experimental results. The numerical curves in Fig. 17 show that during the cycles 4, 5 and 6 (in which the imposed displacement has the biggest value during the experiment) the structural member of HYMOD 1.1 derives a more flexible response than the experimental one, where the derived prediction was in favor of safety. Furthermore, this discrepancy is not noted when using a denser mesh (see HYMOD 1.2), where the proposed algorithm manages to maintain its ability in predicting the overall mechanical behavior of the understudy experiment. From the above overall results, it is evident that the proposed modeling approach manages to capture the experimental results through the use of 8 different meshes, when dealing with a highly nonlinear cyclic loading problem. This numerical finding demonstrates the

numerical robustness of the proposed modeling approach.

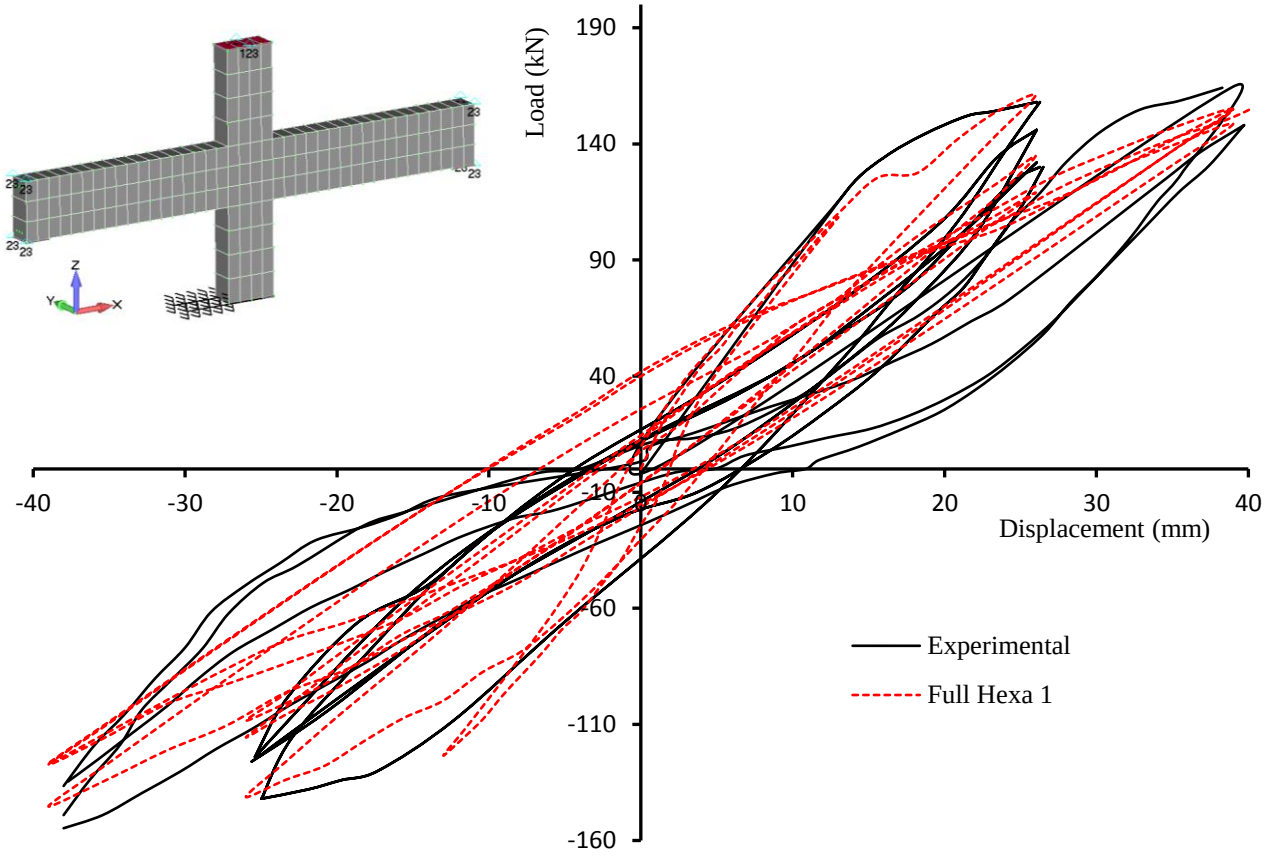

Figure 10. Frame Joint. Comparison between experiment and Full Hexa 1. Complete force-displacement history.

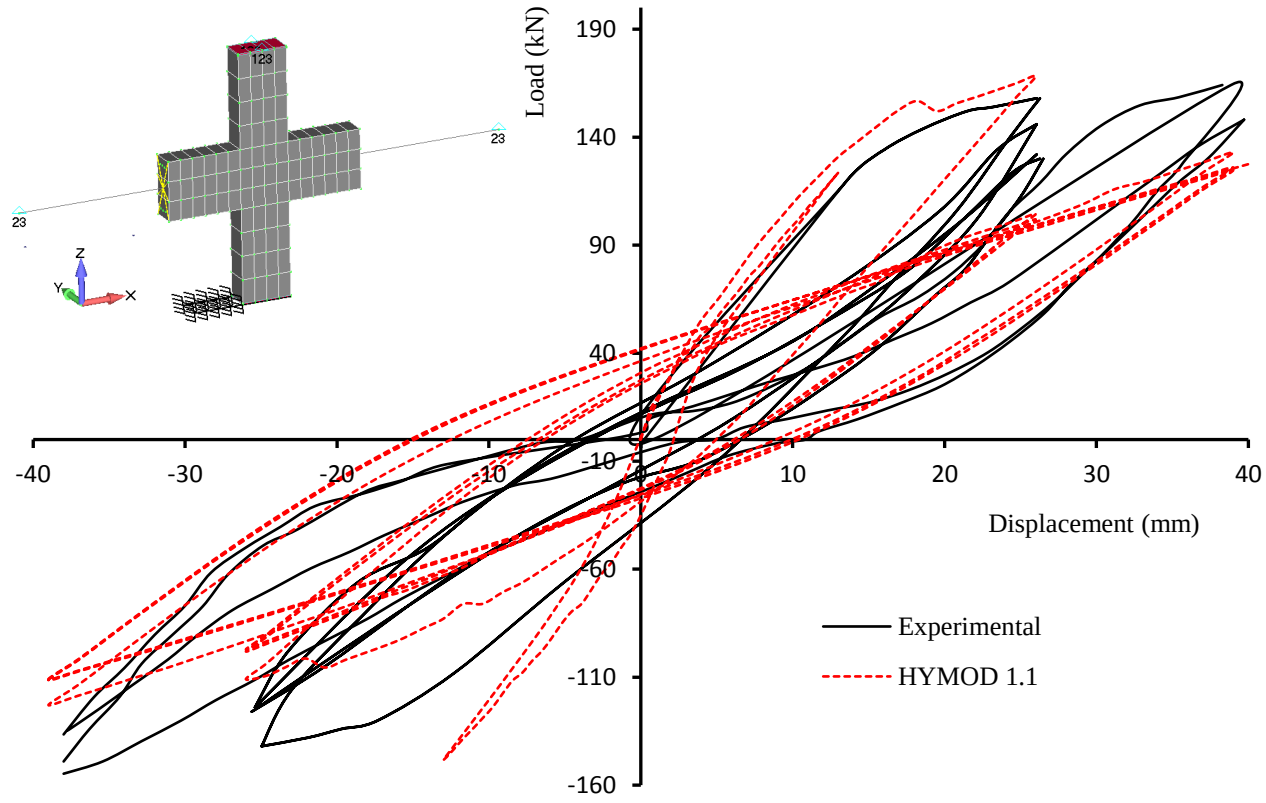

Figure 17. Frame Joint. Comparison between experiment and HYMOD 1.1. Complete force-displacement history.

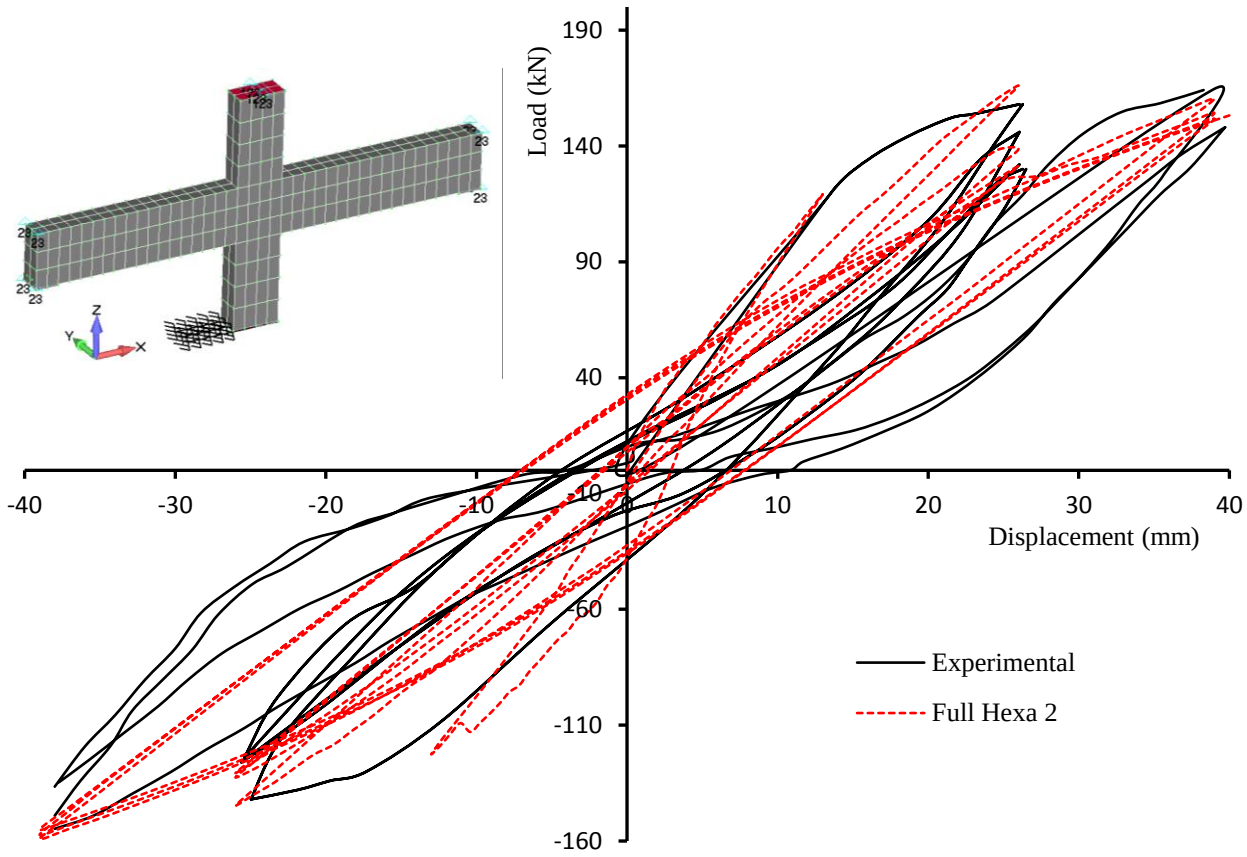

Figure 18. Frame Joint. Comparison between experiment and Full Hexa 2. Complete force-displacement history.

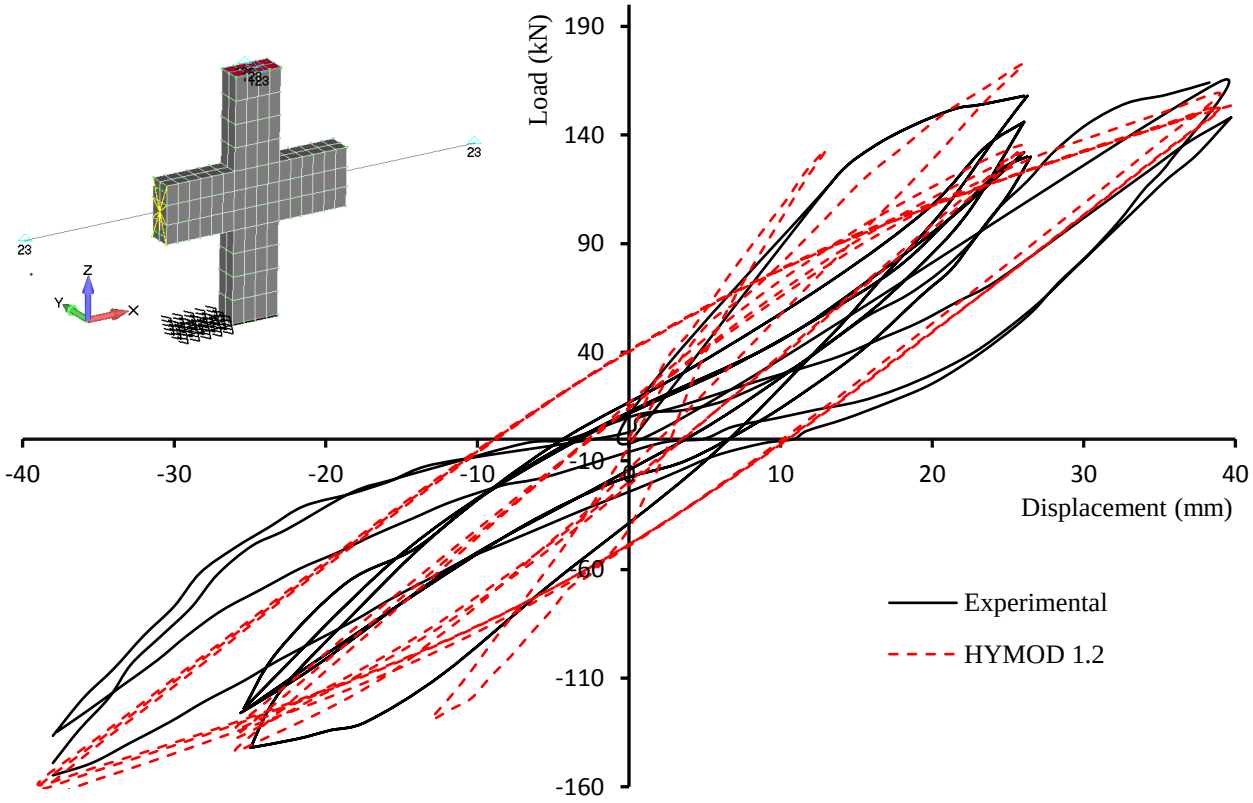

Figure 19. Frame Joint. Comparison between experiment and HYMOD 1.2. Complete force-displacement history.

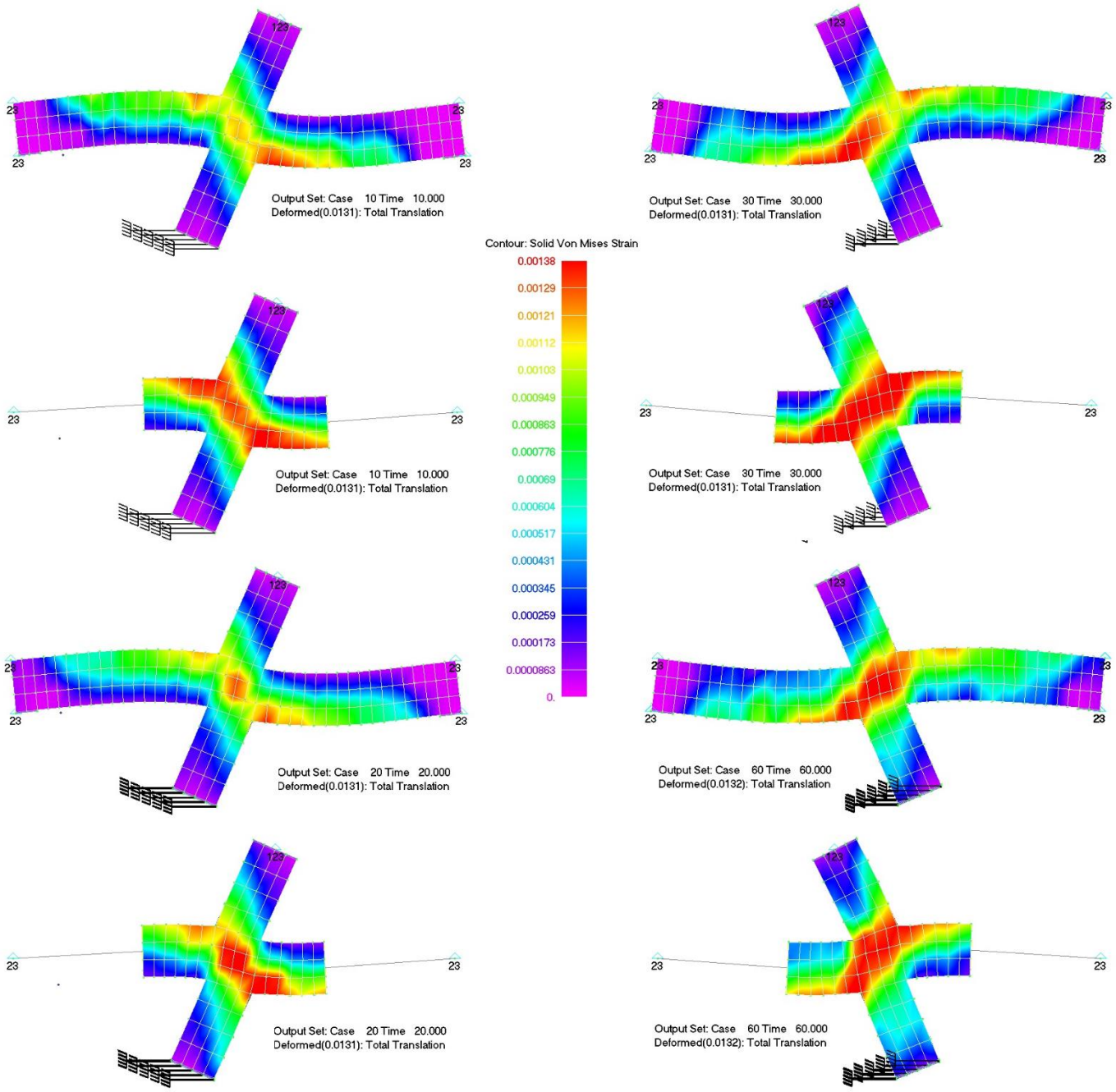

Figure 20. Frame Joint. Von Mises strain contour at load step 10 and 30 (1st cycle of loading) for the refined meshes. Maximum x-axis displacement: ±13 mm.

Table 7 Full Hexa 1 and HYMOD 1.1 numerical results. Comparison of the horizontal load for each cycle.

Loading Cycle	Horizontal Load Full Hexa1 (kN)		Horizontal Load HYMOD 1.1 (kN)		Difference from experimental-Full Hexa 1		Difference from experimental-HYMOD 1.1	
	Positive	Negative	Positive	Negative	Positive (%)	Negative (%)	Positive (%)	Negative (%)
1st	161.04	-141.20	168.24	-110.95	1.93	0.56	6.48	21.87
2nd	134.86	-115.62	104.43	-97.18	7.63	8.24	28.47	22.88
3rd	119.01	-108.37	101.88	-98.12	8.45	12.61	21.63	20.87
4th	155.09	-145.31	132.94	-122.95	5.43	5.64	18.94	20.16
5th	154.88	-127.37	124.70	-111.39	5.56	17.29	23.97	27.67
6th	148.66	-126.97	125.91	-111.02	0.23	7.32	15.50	18.96
				Average	4.87	8.61	19.16	22.07

Table 8 Full Hexa 2 and HYMOD 1.2 numerical results. Comparison of the horizontal load for each cycle.

Loading Cycle	Horizontal Load Full Hexa 2 (kN)		Horizontal Load HYMOD 1.2 (kN)		Difference from experimental-Full Hexa 2		Difference from experimental-HYMOD 1.2	
	Positive	Negative	Positive	Negative	Positive (%)	Negative (%)	Positive (%)	Negative (%)
1st	166.04	-144.75	172.62	-143.48	5.09	1.94	9.25	1.04
2nd	138.76	-132.54	135.11	-137.54	4.96	5.19	7.46	9.16
3rd	131.36	-130.68	131.76	-133.42	1.04	5.38	1.35	7.60
4th	160.39	-159.12	159.07	-165.03	2.20	3.33	3.00	7.16
5th	154.20	-157.33	152.84	-160.80	5.98	2.16	6.80	4.41
6th	151.70	-155.10	152.19	-158.91	1.81	13.21	2.14	15.99
				Average	3.51	5.20	5.00	7.56

For the case of the von Mises strain contours, Fig. 20 illustrates the numerically derived results for the case of the first cycle, when the four refined models are used to analyze the mechanical behavior of the joint. As it can be observed, the same pattern has resulted, as it was discussed for the case of the initial model meshes, thus the numerically predicted strains are not significantly affected by the mesh refinement. The displacement increment used for the solution of the two first models was 40 per loading cycle, while for the case of the models 3 and 4 an 80 displacement increments per cycle was implemented so as to avoid any numerical instabilities due to the finer meshes and the increased number of cracks within the joint domain. It must be noted at this point that using very small in size elements will lead to very dense meshes that will require larger computational times, while lose their practicality in modeling full-scale RC structures due to excessive computational demands. For this reason, a further mesh refinement was deemed unnecessary to be performed and further investigated herein.

5.2 One-Storey RC Frame with a Shear Wall

In this section, the numerical results of a parametric investigation related to the numerical efficiency of the proposed simulation method will be presented for an one-storey RC frame based on the experimental setup of the SERFIN project (Martin et al., 2013). This project deals with the construction of a full-scale four-storey RC building with 25x40cm columns and the retrofit of the middle openings through the use of infill shear walls. Fig. 21 shows the south face of the four-storey RC building that was tested for cyclic loading during the SERFIN project, while the part of the structure that was used to be modeled herein is shown within the framed region of Fig. 21 (see rectangle with dashed line).

Table 9 One-storey frame. Material details.

Material	Young Modulus (GPa)	Hardening Modulus (GPa)	Yielding Stress (MPa)	Compressive Strength (MPa)	Poisson Ratio
Concrete	30	-	-	20	0.2
Steel	200	2.0	400	-	0.3

The main objective in this section is to study the numerical behavior of the proposed modeling approach, whereas the full cyclic modeling of the building will not be presented at this stage. This is a research work that will be presented in a future publication. Therefore, the material properties that are shown in Table 9, are based on the properties reported in (Martin et al., 2013), while the geometry of the RC frame shown in Fig. 22 is according to the specimen's geometrical details found in the project's report. The reinforcement details of the sections used to construct the model shown in Fig. 23, can be depicted in Fig. 22. It must be also noted at this point that, the foundation of the frame was reinforced with 16 mm in diameter bars every 25 cm (bottom and top of the foundation in both directions), while 12 mm stirrups were used to further increase the strength of the foundation. A 3D

representation of the reinforcement grid of the foundation and the rest of the structural members used in the considered model can be seen in Fig. 24. In regards to the concrete cover, all structural members foresaw the use of 20 mm nominal concrete cover.

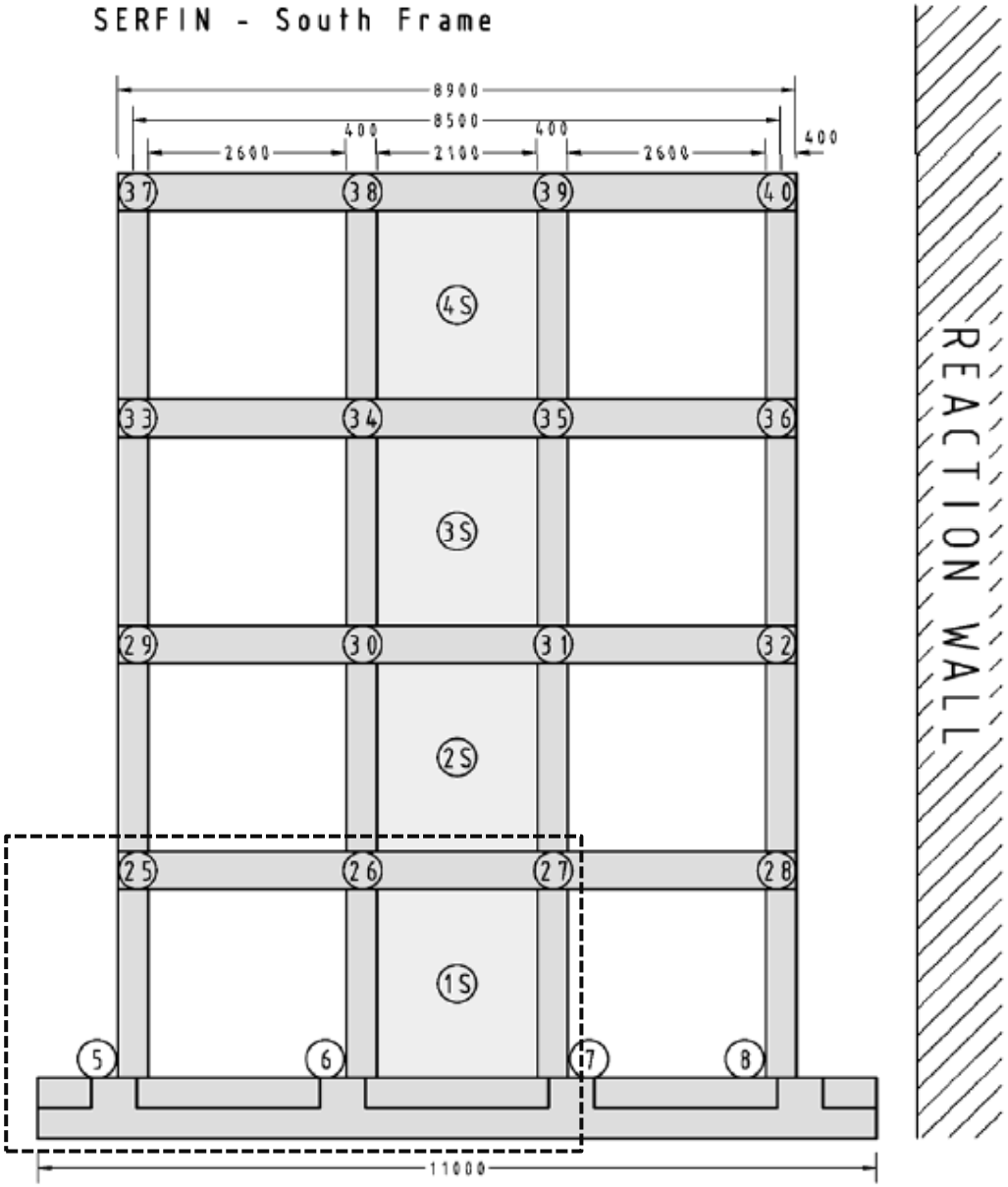

Figure 11. South face of the SERFIN four-storey RC building. (Martin et al., 2013)

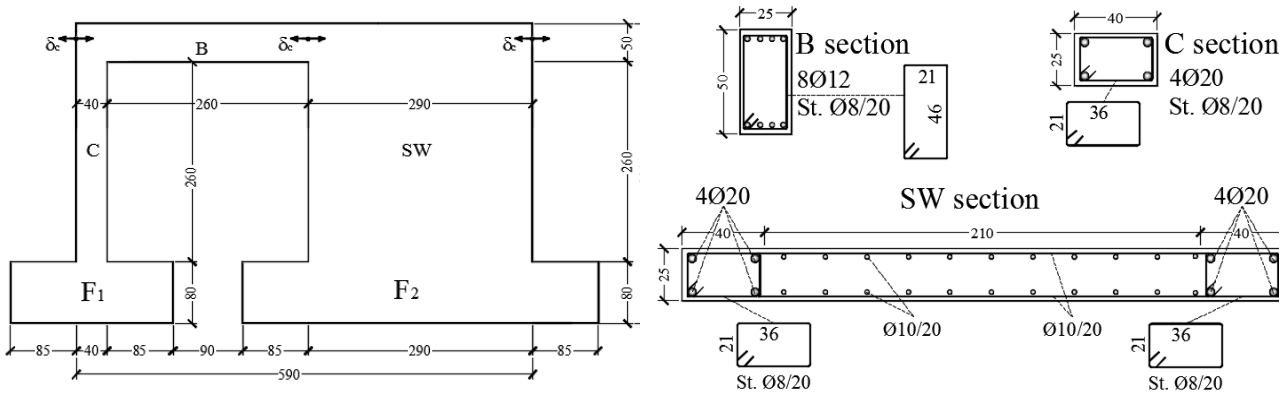

Figure 12. One-storey frame. Geometric (cm) and reinforcement details (Ømm/cm).

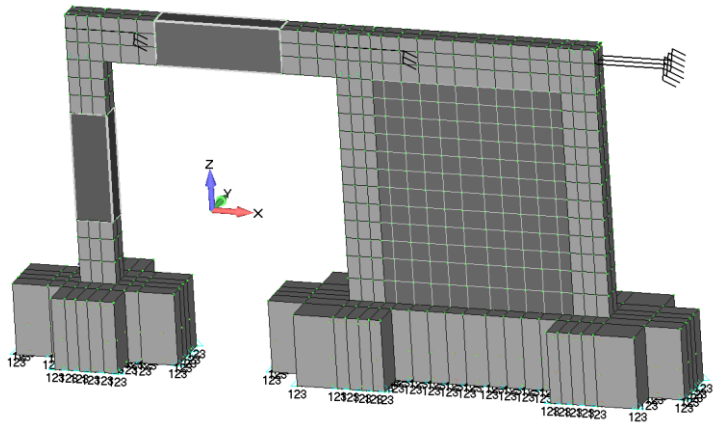

Figure 13. One-storey frame. 3D HYMOD FE mesh.

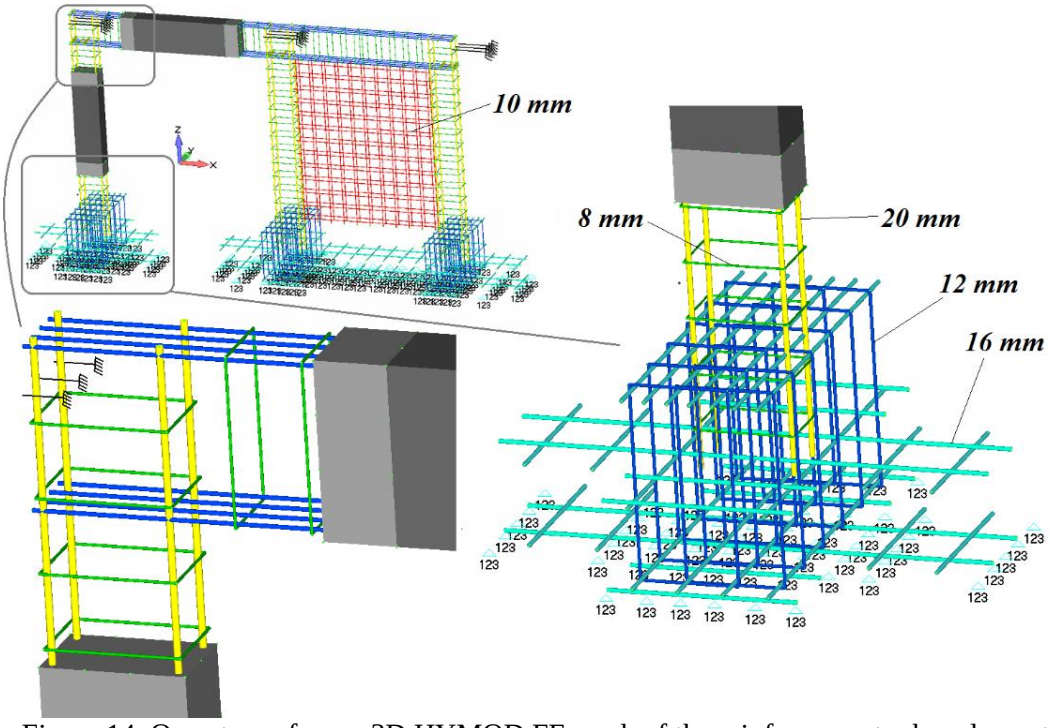

Figure 14. One-storey frame. 3D HYMOD FE mesh of the reinforcement rebar elements.

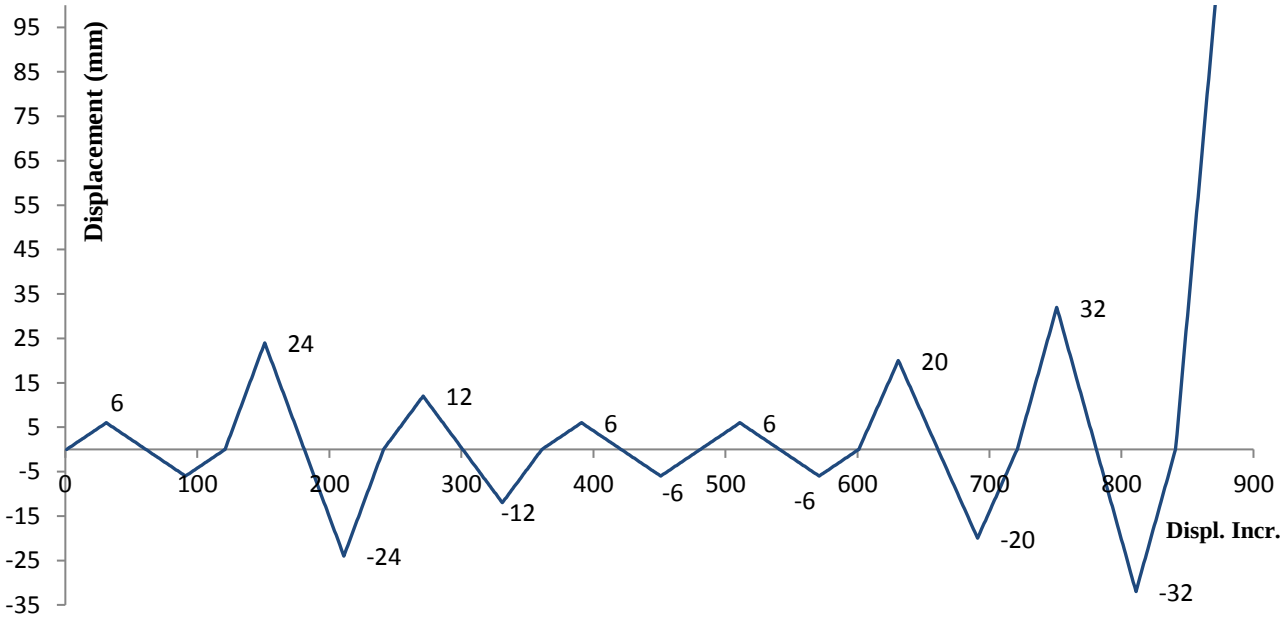

Figure 15. Load history presented in the form of imposed displacements for the one-storey RC frame.

Table 10 FE mesh details of the one-storey RC frame model.

a/a	Model	Hexahedral Elements	Embedded Rebar Elements	RC NBCFB Elements	Total Number of Dofs
1	HYMOD	750	2,594	2	3,474

Figs. 23 and 24 show the FE mesh that was developed for the needs of this numerical investigation. The HYMOD modeling consists of a detailed mesh (hexahedral elements) for the shear dominated structural members (shear wall and structural joints), while the flexural dominated structural members (beams and columns) are simulated by beam elements (reduction level 1, see Markou and Papadrakakis, 2015). The hinge lengths that were used in this model were 50 and 60 cm for the column and beam, respectively. As it can be seen in Figs. 22-24, three points were selected along the beam as the points through which the displacement history was imposed simultaneously, in order to simulate the cyclic loading conditions. The embedded rebar elements were all modeled as beam elements so as to incorporate maximum computational demand. Table 10 shows the details of the developed HYMOD model.

The displacement history that was selected for the needs of this numerical investigation is presented in Fig. 25, where it can be noted that the cyclic displacement history foresees 7 complete cycles, while at the end of the analysis the frame is pushed until a total horizontal displacement of 100 mm. The displacement history diagram in Fig. 25, was developed by using 120 displacement increments per cycle. The displacement increment is also going to be investigated numerically and the corresponding findings will be presented below.

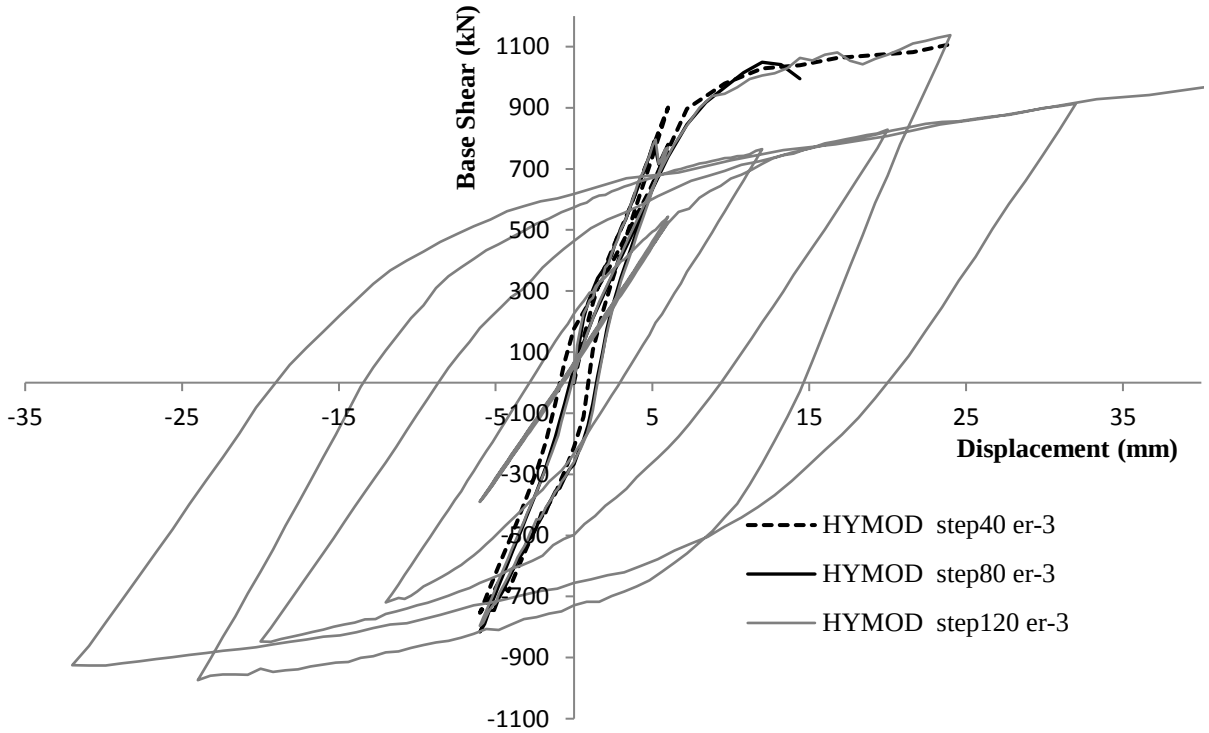

Figure 16. One-storey RC frame. Comparison between different displacement increments with a convergence tolerance 10^{-3}. Complete force-displacement history.

In the first set of analysis the number of displacement increments per loading cycle were 40, 80 and 120, where the convergence tolerance was set to 10^{-3}. As it derived, the two first models with 40 and 80 displacement increments per cycle did not manage to capture the complete displacement history thus failed to converge near the maximum positive displacement magnitude of 24 mm. This is attributed to the loose convergence tolerance at each nonlinear iteration, which was not sufficient to ensure a stable solution, thus the nonlinear analysis reaches to a point where it diverges. On the other hand, when a smaller displacement increment is used, the algorithm manages with the same

convergence tolerance, to converge for all 870 displacement increments, as it is shown in Fig. 26. A stricter convergence tolerance of 10^{-4} led to an improved performance of the 80 displacement increments model, but not of the 40 increments one as is shown in Fig. 27. This numerical finding is attributed to the fact that when using a larger displacement increment, the crack openings within a single step increase significantly, hence can lead to numerical instabilities during the cyclic solution procedure.

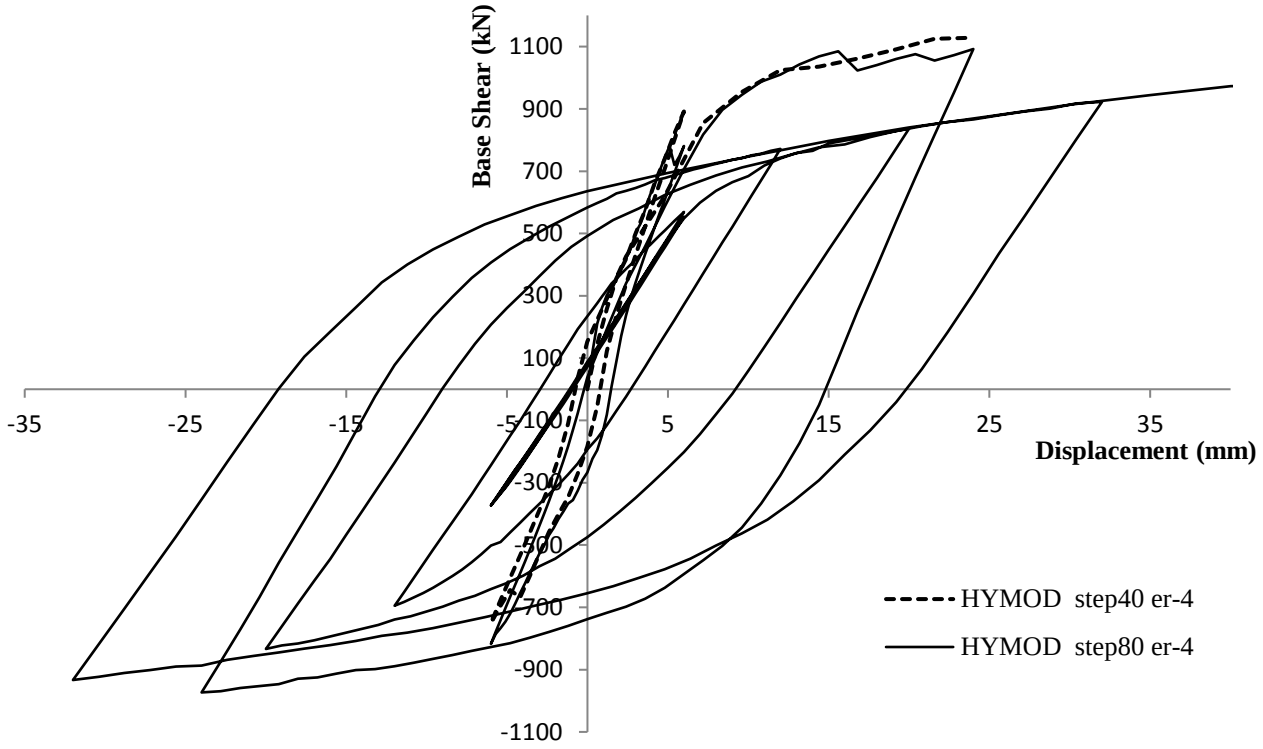

Figure 27. One-storey RC frame. Comparison between different displacement increments with a convergence tolerance 10^{-4}. Complete force-displacement history.

Fig. 28 illustrates the crack patterns for different displacement increments, where the opening and closing of cracks can be seen. It can be observed that the shear wall develops tensile cracks due to the bending moment at the base (output set 1), while diagonal cracks appear at output set 10 (δ = 6 mm) due to shear deformations at the middle of the shear wall. Thereafter, the frame is forced to return to its initial position (output set 20), while cracks start to close from output sets 18 and 19. When the frame is forced to deform along the positive x-axis, cracks develop due to the inverse bending moment and shear deformation that force the structure in developing horizontal and diagonal cracking in a mirrored pattern (see output set 27 in Fig. 28). It must be noted here that the tensile rebars of the beam and shear wall yield when the horizontal displacement during the 2nd loading cycle is larger than 10 mm, a deformation stage where excessive material nonlinearities occur. This numerical response causes the frame to develop large hysteretic loops for the remaining loading cycles, as depicted in Figs. 26 and 27.

Table 11 shows the computational time as it resulted from each analysis, where it can be seen that even in the case of analysis 5, for which a total of 2,285 internal iterations were performed, the total nonlinear analysis time was just 271 seconds with an average error of 7.05×10^{-5}.

Table 11 One-storey RC frame. Computational performance of the five analyses.

a/a	Model	Num. of Displ. Incr. per cycle	Conv. Toler.	Total Displ Incr. Solved	Total Internal Iter.	Average Numerical Error	CPU Time Nonlinear Solution (sec)
1	HYMOD	40	10^{-3}	50	283	9.46×10^{-4}	33
2	HYMOD	80	10^{-3}	92	489	1.04×10^{-3}	58
3	HYMOD	120	10^{-3}	870	2,160	5.31×10^{-4}	259
4	HYMOD	40	10^{-4}	50	414	2.00×10^{-4}	46
5	HYMOD	80	10^{-4}	575	2,285	7.05×10^{-5}	271

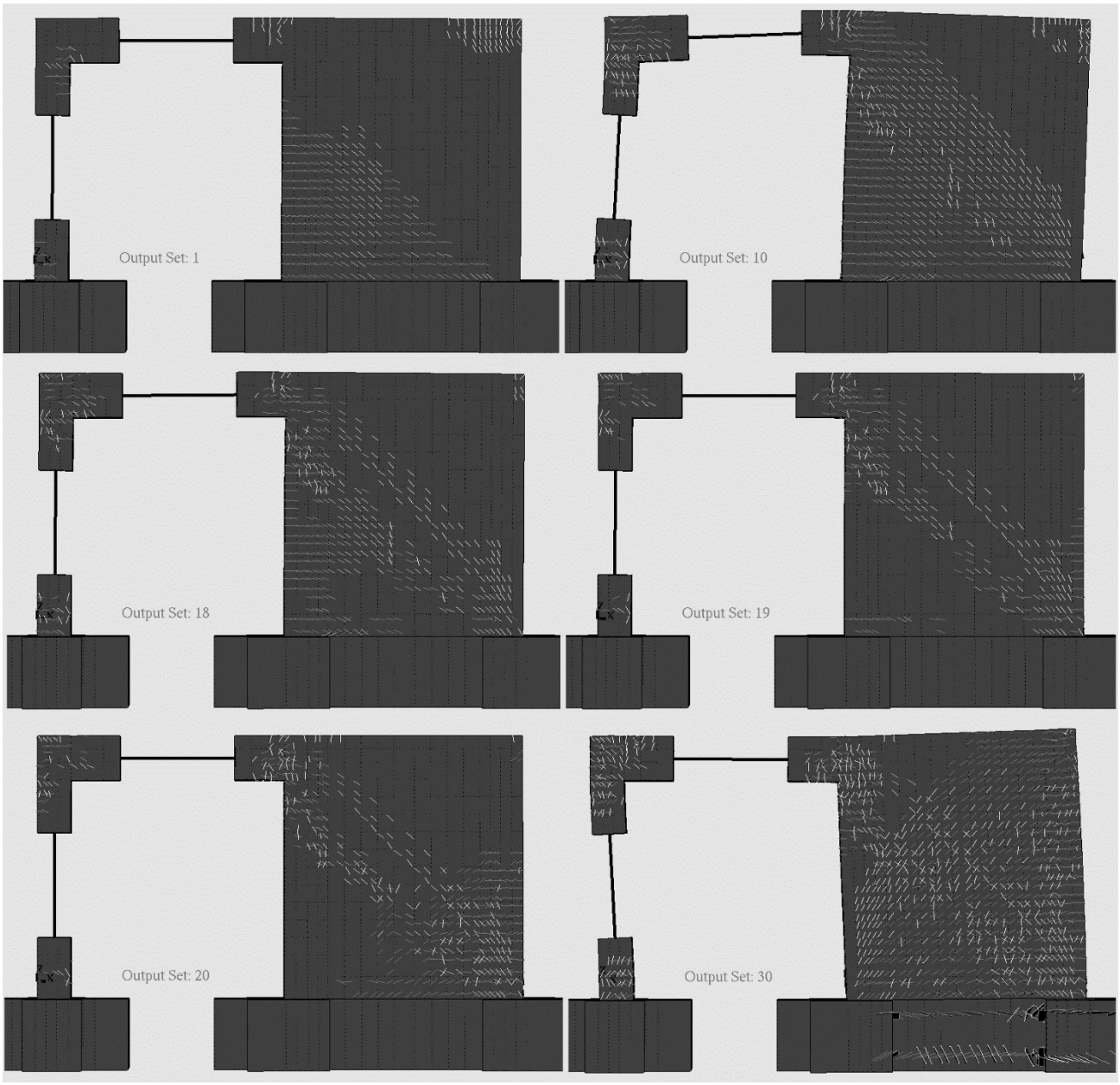

Figure 28. One-storey RC frame. Opening and closing of cracks during the first loading cycle for the first model (40 displacement increments per loading cycle).

5.3 Two-storey RC Frame with Shear Wall

The third model, which is shown in Fig. 29, is a two-storey RC frame which was constructed by adding an extra floor on the model studied in the previous section. The reinforcement details were kept the same for all structural members, as well as the displacement history that was applied to the top beam (Figs. 29 and 30). The main goal of this numerical investigation is to illustrate the ability of the algorithm to solve larger nonlinear numerical problems with the same efficiency and numerical robustness. Furthermore, the HYMOD's limitations in terms of maintaining its accuracy are also investigated herein.

Table 12 shows the FE mesh details of the new models constructed so as to study the proposed numerical model through the simulation of the two-storey RC frame (Fig. 30). The three models investigated were thr: Full Hexa FE mesh with 1,506 hexahedral elements, HYMOD 1 with 1,350 hexahedral elements and the HYMOD 2, with 1,160 hexahedral elements. The corresponding number of the embedded rebar elements that were used to model the reinforcement were 4,544, 5,134 and 3,348 for the Full Hexa, HYMOD 1 and HYMOD 2 models, respectively (see Table 12). The reduction of the total number of dofs for HYMOD 1 and 2 were 13.96% and 26.54%, respectively. In order to

intensify the computational demand of this numerical problem, the convergence tolerance was set to 10^{-5}, where nine analyses were performed for the needs of this numerical investigation.

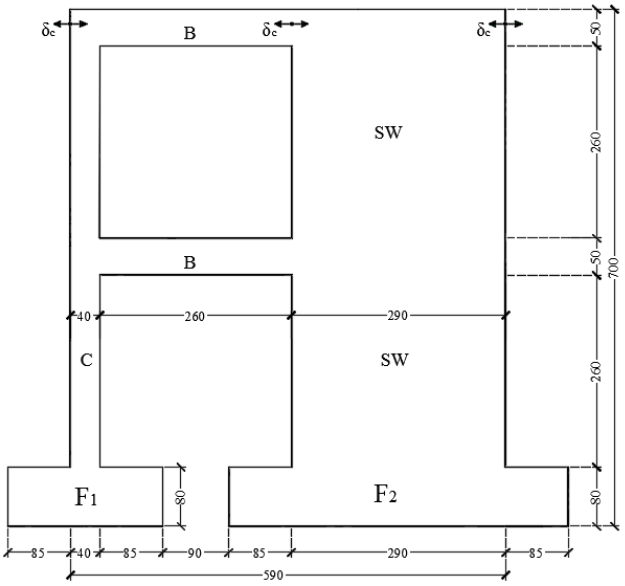

Figure 29. Two-storey RC frame. Geometric details.

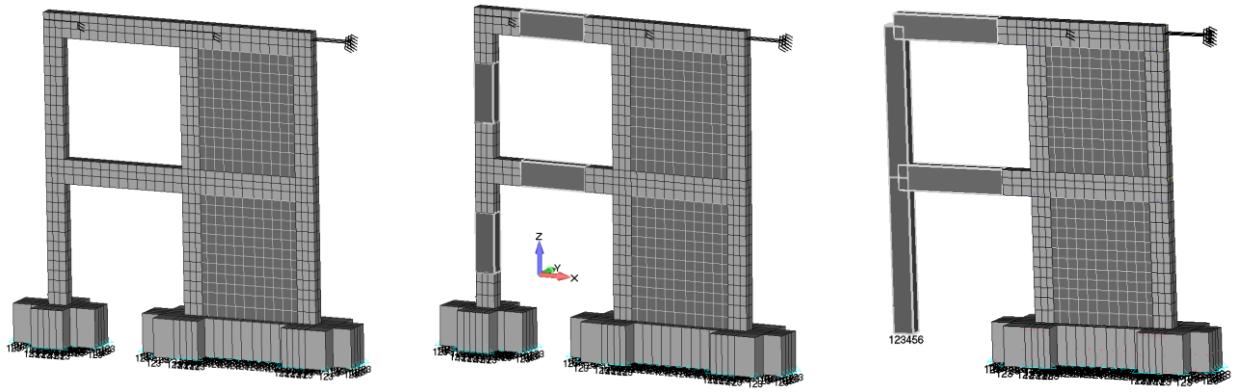

a. b. c.

Figure 30. Two-storey RC frame. FE meshes of a. Full Hexa, b. HYMOD 1 and c. HYMOD 2 models.

Table 12 FE mesh details of the 1-storey RC frame model.

a/a	Model	Hexahedral Elements	Embedded Rebar Elements	RC NBCFB Elements	Total Number of Dofs	Dof Reduction (%)
1	Full Hexa	1,506	4,544	-	7,392	-
2	HYMOD 1	1,350	4,134	4	6,360	13.96
3	HYMOD 2	1,160	3,348	4	5,430	26.54

Fig. 31 shows the force-displacement history as it resulted from the six analyses (Full Hexa and HYMOD 1 meshes) that were performed by using a constant convergence tolerance of 10^{-5} and three different displacement increments (40, 80 and 120 displacement increments per loading cycle). It is interesting to note here that for the case of the two-storey RC frame, all three cases (contrary to the obtained results in the one-storey test example), managed to provide with the complete solution. This finding is attributed to the fact that the structure in the case of the two-storey RC frame is taller, therefore, the shear deformation is smaller, while at the same time the crack openings that were computed were less (given that the same displacement history was applied in both models, one- and two-storey RC frames; therefore, the shortest structure is expected to develop a larger shear deformation and higher crack openings). The comparison between the resulted force-displacement hysteretic loops of HYMOD 1 and the Full Hexa models, as it is shown in Fig. 31, revealed that the two models derived almost identical curves, illustrating once more the robustness of the proposed modeling approach.

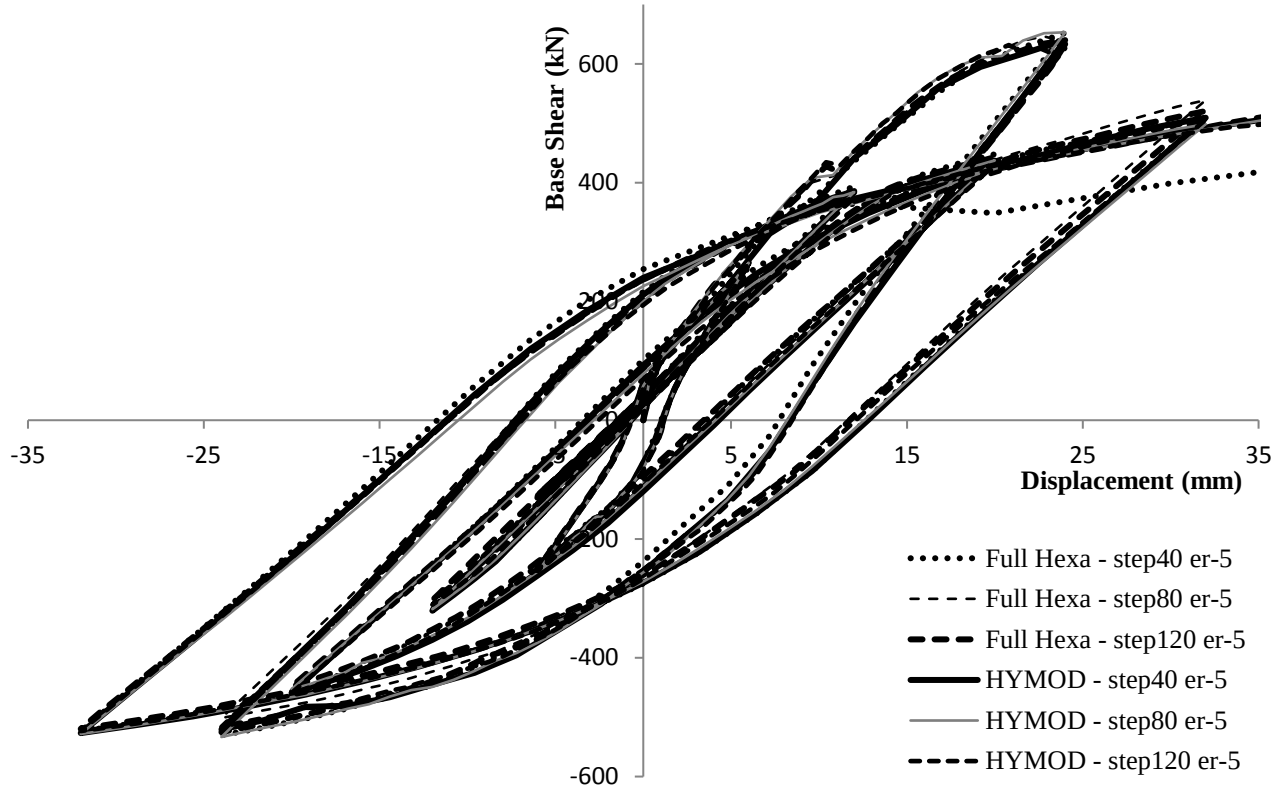

Figure 17. Two-storey RC frame. Comparison between HYMOD 1 and Full Hexa for different displacement increments with a convergence tolerance 10^{-5}. Complete force-displacement history.

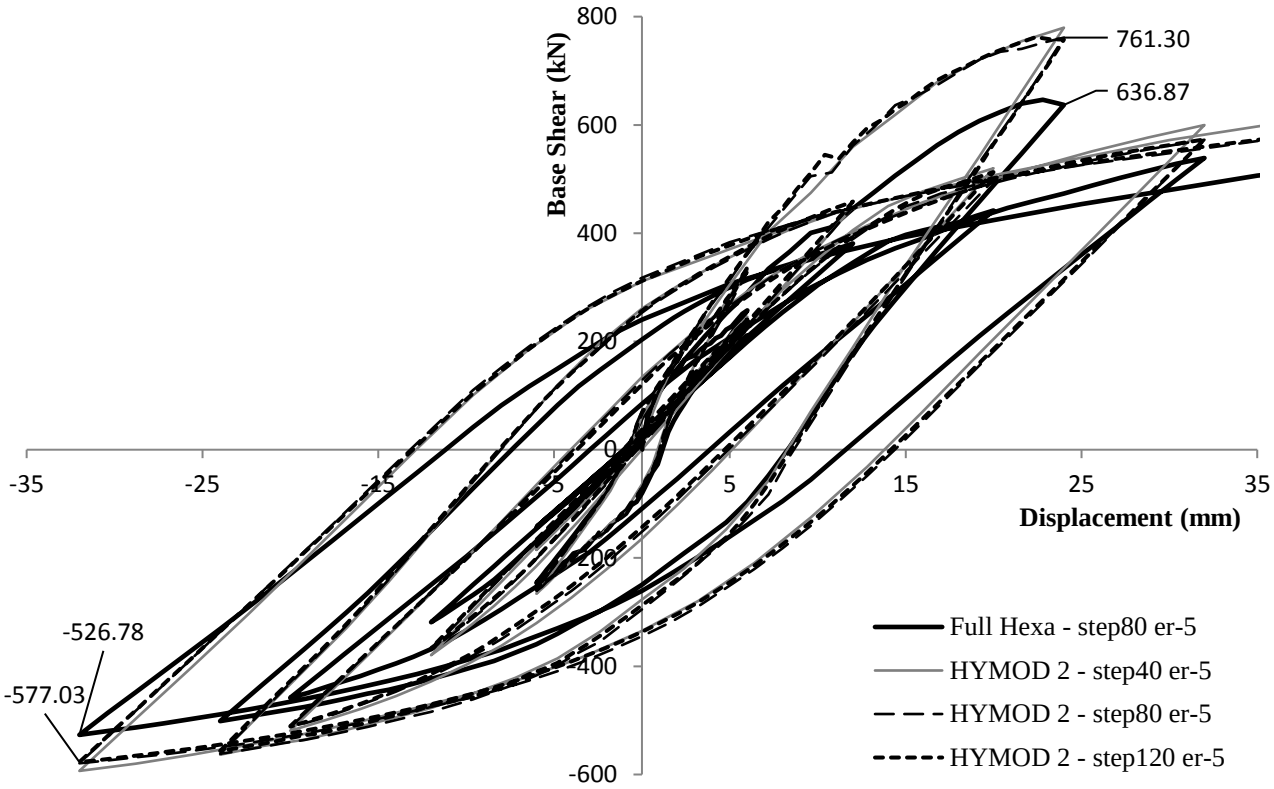

Figure 18. Two-storey RC frame. Comparison between HYMOD 2 and Full Hexa for different displacement increments with a convergence tolerance 10^{-5}. Complete force-displacement history.

An additional finding that can be depicted in Fig. 31, is the drop of the overall strength that the full Hexa model exhibited after all the displacement cycles were applied in the case of the 40 displacement increments per loading cycle was used. When using a larger displacement increment, a decreased

strength is observed as a result of the deterioration of the concrete material that can lead to the decrease of the overall strength. Furthermore, it can also be seen here that the HYMOD 1 mesh provides the required numerical accuracy and robustness in overcoming this numerical phenomenon, whereas all three HYMOD 1 analyses presented in Fig. 31 are almost identical to the Full Hexa model that uses the two displacement increments of 80 and 120 displacement increments per loading cycle.

Fig. 32 depicts the force-displacement curves that resulted from the Full Hexa and the HYMOD 2 models. It is evident that the HYMOD 2 mesh derives a stiffer behavior at the initial cycles of the loading history, obtaining a maximum base shear of 761 kN, which is 19% larger than the corresponding value that was computed by the Full Hexa and HYMOD 1 models. This numerical finding is attributed to the stiffer NBCFB FEs that do not take into account the full magnitude of nonlinearities that occur at the beam-column joint and at the base of the column. After the first 4 loading cycles are solved (where the HYMOD 2 demonstrates a stiffer behavior) the curve manages to capture the Full Hexa curve with a 9.7% accuracy highlighting the ability of the method to maintain an acceptable accuracy, even in the case of high mesh reduction levels.

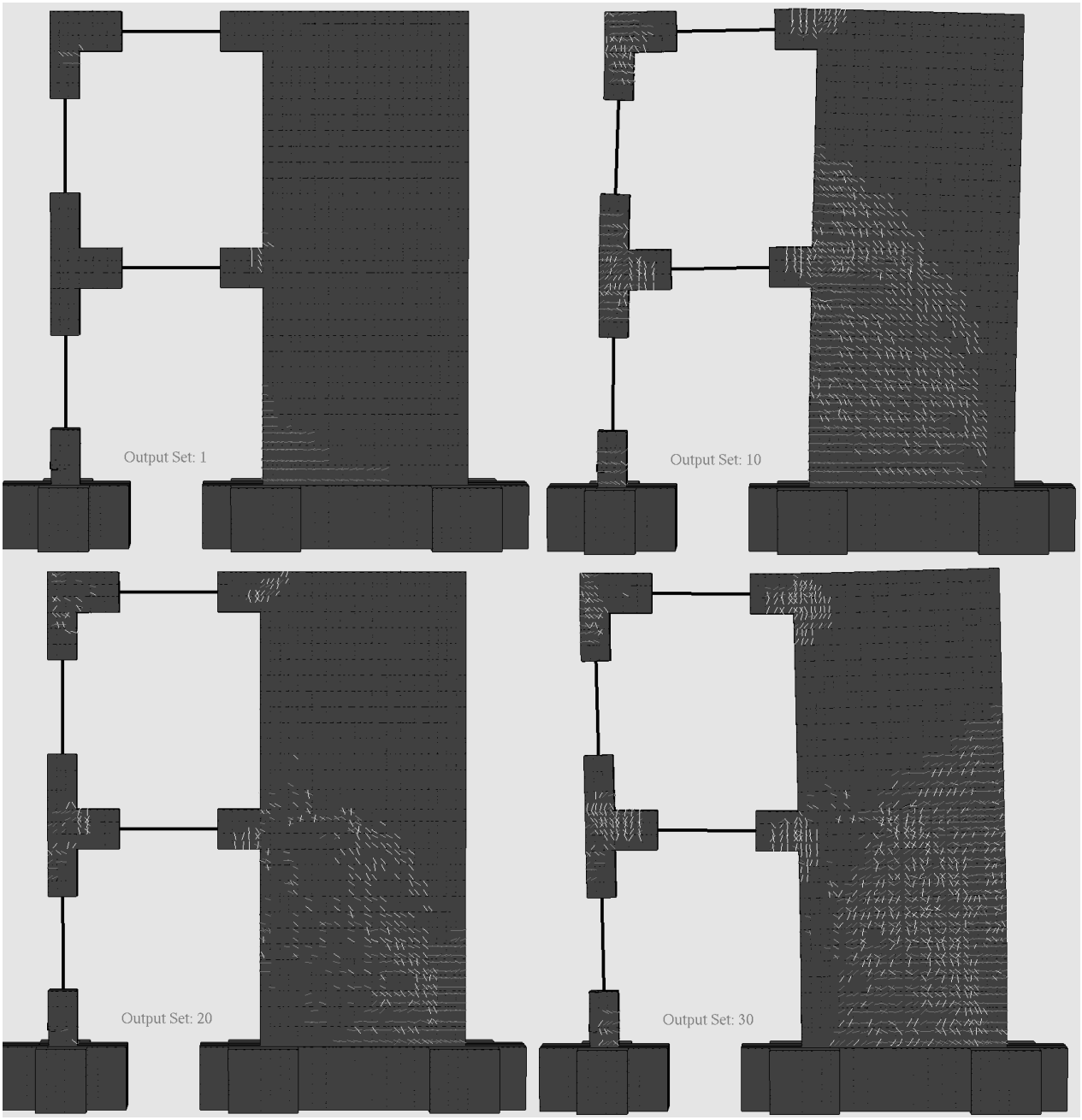

Figure 19. 2-storey RC frame. Opening and closing of cracks during the 1st loading cycle for the first model (40 displacement increments per loading cycle).

Furthermore, for the case of this numerical investigation, it was found that the crack opening and closing algorithm managed once more to successfully capture this numerically demanding and unstable process providing the additional numerical stability that is required to solve this highly nonlinear numerical problem. Fig. 33 shows the opening and closing of cracks for the 1st loading cycle of the two-storey RC frame as it resulted from the analysis. It is evident that in the case of the two-storey RC frame the number of crack openings is significantly lower than that predicted in the one-storey RC frame by HYMOD 1, especially in the case of displacement increment 1 (Fig. 28). This justifies the previous conclusion in regards to the main reason why HYMOD 1 for the one-storey RC frame did not manage to attain the complete displacement history when the displacement increments per loading cycle was set to 40.

Table 13 Two-storey RC frame. Computational performance of the three analyses.

a/a	Model	Num. of Displ. Incr. per cycle	Total Displ Incr. Solved	Total Internal Iter.	Average Num. Error	CPU Time Nonlinear Solution (minutes)	Reduction in CPU Nonlinear Solution (%)
1	Full Hexa	40	290	2,313	$2.07x10^{-5}$	9.6	-
2	Full Hexa	80	580	3,975	$1.11x10^{-5}$	16.1	-
3	Full Hexa	120	870	5,451	$9.45x10^{-6}$	22.75	-
4	HYMOD 1	40	286	2,118	$1.546x10^{-5}$	7.3	23.63
5	HYMOD 1	80	580	3,821	$9.39x10^{-6}$	14.3	11.18
6	HYMOD 1	120	870	5,136	$7.31x10^{-6}$	19.5	14.29
7	HYMOD 2	40	290	2,092	$1.32\ x10^{-5}$	5.47	43.03
8	HYMOD 2	80	580	3,733	$9.51\ x10^{-6}$	9.6	40.37
9	HYMOD 2	120	870	4,990	$7.98x10^{-6}$	13.1	42.42

Table 13 shows the computational performance data obtained from the nine analyses. The computed average numerical error per internal iteration, for the case of the Full Hexa model, was found to be lower than $2.1x10^{-5}$, while the HYMOD 1 managed to result an average numerical error per iteration that was less than $1.6x10^{-5}$. The same trend resulted for the case of the HYMOD 2 model, which was the most computationally efficient model. This is also evident from the computed average number of internal iterations per displacement increment, which was always smaller in the case of the HYMOD 1 and 2, in comparison to the full Hexa model. The proposed HYMOD model managed to maintain a low internal iteration per displacement increment (average: 7.4, 6.6 and 5.9 for the HYMOD 1 mesh with 40, 80 and 120 displacement increments, respectively), while the maximum required computational time for HYMOD 1 was 19.5 minutes for the solution of 5,136 internal iterations. The corresponding performance for the case of HYMOD 2 model was 7.2, 6.4 and 5.7 average internal iterations per displacement increment and a 0.156 seconds overall average required computational solution time per internal iteration. The overall average for the case of the HYMOD 1 model was 0.223 seconds per internal iteration. On the other hand, the Full Hexa models had an average internal iteration per displacement increment equal to 7.96, 6.85 and 6.27 for the case of 40, 80 and 120 displacement increments per loading cycle, respectively. The corresponding average computational time per internal iteration was 0.248 seconds, which is 10% slower compared to the HYMOD 1 and 37.1% slower than the HYMOD 2.

The above numerical finding is attributed to the decreased number of hexahedral elements, the decrease of the required internal iterations per displacement increment and the lower number of embedded rebars, when the proposed HYMOD approach is implemented. In general, the overall decrease in the computational time is equal or larger than the decrease of the dof achieved according to the reduction of the full hexahedral mesh. Furthermore, the numerical model HYMOD 2 manages to reduce the nonlinear solution time by 42%, which corresponds to a 158% increase in the expected computational gain by just applying a corresponding dof decrease of a mere 26.54%. This demonstrates the computational efficiency boost that the nonlinear cyclic solution procedure can develop when the HYMOD approach is applied.

6. Conclusions

The hybrid finite element modeling approach presented in this work for the nonlinear simulation of RC structures under cyclic loading conditions, is a compromise between a detailed finite element model and the simplified beam-type model (Markou and Papadrakakis, 2015). In order to decrease the computational demand during a cyclic nonlinear analysis of a RC structure, without decreasing the level of numerical accuracy, the use of the HYMOD approach is adopted herein that foresees the use of the detailed modeling with hexahedral elements for discretizing the concrete domain and embedded rebar elements for the reinforcement, which is used to discretize the parts of the structure that undergo shear dominated deformations, while the rest of the structural members are discretized through the use of beam-column finite elements. The HYMOD approach was integrated for the needs of this research work with the cyclic material model proposed by Mourlas et al. 2017.

The numerical investigation performed in a number of FE models revealed the ability of the proposed HYMOD approach to accurately predict the nonlinear response of RC structural members under cyclic loading conditions, with a reduced computational effort. The proposed formulation was found to be computationally robust since it does not require any special algorithmic procedure for its implementation. The integration of the HYMOD algorithm with the cyclic concrete material model further fortified the numerical method with additional numerical stability, which is essential when the cracks begin to open and close (Mourlas et al., 2017). The numerical results revealed that the proposed simulation manages to retain a low ratio of internal iterations per displacement increment thus further reducing the computational demand of the nonlinear analysis. Furthermore, the mesh sensitivity investigation presented in section 5.1 revealed that the proposed modeling approach manages to maintain its accuracy and ability in capturing the mechanical behavior of RC structural members that are tested under cyclic loading conditions for cases where the mesh size is modified within a recommended margin of 10 to 25 cm. Additionally, it was concluded that the proposed method's numerical ability to capture the experimental data, is not significantly affected when different reduction levels are implemented.

By accounting the numerical findings obtained in sections 5.2 and 5.3 of this research work, it is safe to conclude that the proposed numerical simulation method can provide with the ability to study the cyclic nonlinear simulation of full-scale RC structures, thus this cumbersome numerical modeling problem is now feasible. Therefore, this simulation task can now be achieved at an affordable computational effort without the need of powerful computational resources, while maintaining at the same time the desired accuracy during the cyclic nonlinear analysis.

7. Acknowledgement

The authors would like to acknowledge the financial support provided by the European Research Council Advanced Grant "MASTER-Mastering the computational challenges in numerical modeling and optimum design of CNT reinforced composites" (ERC-2011-ADG 20110209).

References

Ali Bark H., Markou G., Mourlas Ch. and Papadrakakis M., "Seismic Assessment of a 5-Storey Retrofitted RC Building", ECCOMAS Congress, VII European Congress on Computational Methods in Applied Sciences and Engineering, Crete Island, Greece, 5–10 June 2016.

Blanco P.J., Feijoo R.A. and Urquiza S.A. (2007), "A unified variational approach for coupling 3D–1D models and its blood flow applications", Comput. Methods Appl. Mech. Engrg., Vol. 196, pp. 4391:4410.

Blanco P.J., Feijoo R.A. and Urquiza S.A. (2008), "A variational approach for coupling incompatible structural models", Comput. Methods Appl. Mech. Engrg., Vol. 197, pp. 1577:1602.

Bournival S., Cuillière J.-C. and François V. (2010a), "A mesh-based method for coupling 1D and 3D elements." Advances in Engineering Software, Vol. 41, pp. 838:858.

Bournival S., Cuillière J.-C. and François V. (2010b), "A mesh-geometry-based solution to mixed-

dimensional coupling", Computer-Aided Design, Vol. 42, pp. 509:522.
Červenka J. and Papanikolaou V.K. (2008), Three dimensional combined fracture-plastic material model for concrete, International Journal of Plasticity, 24(12) 2192-2220.
Del Toro Rivera R. (1988). "Behavior of reinforced concrete beam column joints under alternated loading", Ph.D. thesis, Ecole Nationale des Ponts et Chaussées, Paris.
Formaggia L., Gerbeau J.F., Nobile F. and Quarteroni A. (2001), "On the coupling of 3D and 1D Navier–Stokes equations for flow problems in compliant vessels", Comput. Methods Appl. Mech. Engrg., Vol. 191, pp. 561:582.
Gonzalez-Vidosa F., Kotsovos M.D. and Pavlovic M.N. (1991), A three-dimensional nonlinear finite-element model for structural concrete. Part 1: main features and objectivity study; and Part 2: generality study, Proceedings of the Institution of Civil Engineers, Part 2, Research and Theory, Vol. 91, pp. 517-544.
Hartl H. (2002), "Development of a continuum mechanics based tool for 3D FEA of RC Structures and application to problems of soil structure interaction." Ph.D. thesis, Faculty of Civil Engineering, Graz Univ. of Technology.
Huang J. (2004), "Numerical solution of the elastic body-plate problem by nonoverlapping domain decomposition type techniques", Math. Comput., Vol. 73, pp. 19:34.
Kotsovos M.D. and Pavlovic M.N. (1995), Structural concrete, finite element analysis for limit state design, Thomas Telford, London, UK.
Kozlov V.A. and Maz'ya, V.A. (2001), "Fields in non-degenerate 1D–3D elastic multi-structures", Quart. J. Mech. Appl. Math., Vol. 54, pp. 177:212.
Lykidis G.Ch. and Spiliopoulos K.V. (2008), "3D solid finite element analysis of cyclically loaded RC structures allowing embedded reinforcement slippage", Journal of Structural Engineering-ASCE, 134(4), 629-638.
Markou G, Papadrakakis M. (2013), "Computationally efficient 3D finite element modeling of RC structures. Computers and Concrete", 12(4), 443–98.
Markou G. and Papadrakakis M. (2015), "A Simplified and Efficient Hybrid Finite Element Model (HYMOD) for Non-Linear 3D Simulation of RC Structures", Engineering Computations, Vol. 32 (5), pp. 1477-1524.
Martin P., Fabio T., Javier M. R., Christis Ch., Nicholas K., Toula O., Panayiotis R., Panagiotis K., Telemachos P., Antonis K. (2013), "Seismic Retrofitting of RC Frames with RC Infilling (SERFIN Project)", European Commission, Joint Research Center, Institute of the Protection and Security of Citizens.
Mata P., Barbat A.H. and Oller S. (2008), "Two-scale approach for the nonlinear dynamic analysis of RC structures with local non-prismatic parts", Eng. Struct.,Vol. 30(12), pp. 3667:3680.
Menegotto M., and Pinto P. E. (1973). "Method of analysis for cyclically loaded reinforced concrete plane frames including changes in geometry and non-elastic behavior of elements under combined normal force and bending." Proceedings, IABSE Symposium on Resistance and Ultimate Deformability of Structures Acted on by Well Defined Repeated Loads, Lisbon, Portugal, 15–22.
Mourlas Ch., Papadrakakis M. and Markou G., "A computationally efficient model for the cyclic behavior of reinforced concrete structural members", Engineering Structures. Vol. 141, 97-125, 2017.
Nazarov S.A. (1996), "Junctions of singularly degenerating domains with different limit dimensions I", J. Math. Sci., Vol. 80, pp. 1989:2034.
Nazarov S.A. (1999), "Junctions of singularly degenerating domains with different limit dimensions II", J. Math. Sci. Vol. 97, pp. 4085:4108.
Papanikolaou V.K. and Kappos A.J. (2009), "Numerical study of confinement effectiveness in solid and hollow reinforced concrete bridge piers: Part 1: Methodology and Part 2: Analysis results and discussion. Engineering Structures", Vol. 87, 1427–1439, 1440-1450, 2009.
Rashid Y.M. (1968), Ultimate strength analysis of prestressed concrete vessels, Nucl Eng and Des, Vol. 7, pp. 334-344.
Urquiza S.A., Blanco P.J., Venere M.J. and Feijoo R.A. (2006), "Multidimensional modelling for the

carotid artery blood flow", Comput. Methods Appl. Mech. Engrg., Vol. 195, pp. 4002:4017.
Willam K. J. and Warnke E. P., (1974), "Constitutive model for the triaxial behaviour of concrete", Seminar on concrete structures subjected to triaxial stresses, Instituto Sperimentale Modeli e Strutture, Bergamo, Paper III-1.